### Title

Characterizing Sierra Nevada Snowpack Using Variable-Resolution CESM




### Journal

Journal of Applied Meteorology and Climatology, 55(1)

### ISSN

1558-8424



### Authors

Rhoades, Alan M
Huang, Xingying
Ullrich, Paul A
et al.



### Publication Date

2016

### DOI

10.1175/jamc-d-15-0156.1

Peer reviewed

# Characterizing Sierra Nevada Snowpack Using Variable-Resolution CESM

ALAN M. RHOADES, XINGYING HUANG, AND PAUL A. ULLRICH

University of California, Davis, Davis, California

COLIN M. ZARZYCKI

National Center for Atmospheric Research,* Boulder, Colorado

* The National Center for Atmospheric Research is sponsored by the National Science Foundation.

Corresponding author address: Alan M. Rhoades, University of California, Davis, Dept. of Land, Air, and Water Resources, 1110 Plant and Environmental Sciences Bldg., One Shields Ave., Davis, CA 95616. E-mail: amrhoades@ucdavis.edu

Abstract

The location, timing, and intermittency of precipitation in California make the state integrally reliant on winter-season snowpack accumulation to maintain its economic and agricultural livelihood. Of particular concern is that winter-season snowpack has shown a net decline across the western United States over the past 50 years, resulting in major uncertainty in water-resource management heading into the next century. Cutting-edge tools are available to help navigate and preemptively plan for these uncertainties. This paper uses a next-generation modeling technique—variable-resolution global climate modeling within the Community Earth System Model (VR-CESM)—at horizontal resolutions of 0.125° (14 km) and 0.25° (28 km). VR-CESM provides the means to include dynamically large-scale atmosphere–ocean drivers, to limit model bias, and to provide more accurate representations of regional topography while doing so in a more computationally efficient manner than can be achieved with conventional general circulation models. This paper validates VR-CESM at climatological and seasonal time scales for Sierra Nevada snowpack metrics by comparing them with the “Daymet,” “Cal-Adapt,” NARR, NCEP, and North American Land Data Assimilation System (NLDAS) reanalysis datasets, the MODIS remote sensing dataset, the SNOTEL observational dataset, a standard-practice global climate model (CESM), and a regional climate model (WRF Model) dataset. Overall, given California’s complex terrain and intermittent precipitation and that both of the VR-CESM simulations were only constrained by prescribed sea surface temperatures and data on sea ice extent, a 0.68 centered Pearson product-moment correlation, a negative mean SWE bias of <7 mm, an interquartile range well within the values exhibited in the reanalysis datasets, and a mean December–February extent of snow cover that is within 7% of the expected MODIS value together make apparent the efficacy of the VR-CESM framework.

Keywords: Climate models; Land surface model; Model evaluation/performance; Multigrid models

## 1. Introduction

California receives one-half of its total annual precipitation in 5–15 days of the year, making its precipitation patterns some of the most intermittent in the United States (Dettinger et al. 2011). Important is that most of the state's precipitation falls during the winter months [December–February (DJF)] and that two-thirds of it precipitates in the northern and mountainous parts of the state (Wise 2012). The precipitation that falls in the mountainous region largely accumulates as snow (Pandey et al. 1999). Thus, winter snowpack acts as a natural surface reservoir for water that is then released during dry portions of the year. Snowpack provides approximately three-quarters of the annual freshwater supply in the western United States (Palmer 1988; Cayan 1996), and 60% of California's developed water supply originates from the snowpack-dominated Sierra Nevada (Bales et al. 2011). Along with the Colorado River, this natural store of water contributes to the maintenance of California's economy and its status as one of the largest agricultural providers in the world (Tanaka et al. 2006; Hanak and Lund 2012). These water reserves also provide up to 21% of the energy found within California's diverse energy portfolio via hydroelectric plants (Stewart 1996). Therefore, the integrity of California's economy, and its agricultural identity, are largely dependent on ample snowpack accumulation in the Sierra Nevada.

A major cause of interannual variability in winter precipitation in California and the greater western United States is global teleconnections. Teleconnections are recurrent and persistent atmosphere–ocean patterns that affect large swaths of latitudinal and longitudinal bands (Wallace and Gutzler 1981; Glantz et al. 1991). They are important from a water-resources perspective because they determine overall temperature, precipitation, and snowpack trends within California. Atmosphere–ocean climate interactions have been found to cause annual precipitation to vary by 20%–45% in the western United States (Dettinger et al. 1998); such interactions include El Niño–Southern Oscillation (ENSO), the Pacific decadal oscillation (PDO), the Pacific–North American (PNA) pattern, the North American monsoon, and the Aleutian low, as well as more short-term events known as atmospheric rivers (AR) that are equatorially generated whiplike water vapor bands (Dettinger et al. 1998; Cayan et al. 1999; Ralph et al. 2004; Dettinger 2011; Wise 2012; Guan et al. 2013; Fang et al. 2014). The internal variability associated with teleconnections modulates the spatial and temporal variability of strong precipitation events in the western United States (Wise 2012). Therefore, teleconnection modulation, on both yearly and decadal time frames, has a direct impact on the amount of total seasonal snowpack deposited in the Sierra Nevada. This modulation is also essential in resolving historical trends as well as projecting future snowpack tendencies. For example, ARs alone account for ~30%–40% of seasonal snowpack accumulation in the Sierra

Nevada (Guan et al. 2010). Thus, a representation of global processes, ideally with a global climate model (GCM), is necessary to accurately account for California's temperature, precipitation, and snowpack trends.

To observe how this crucial natural freshwater reserve is characterized, both spatially and temporally, snowpack metrics such as snow water equivalent (SWE), snow centroid date (SCD), and the extent of snow cover (SNOWC) have been developed to quantify the patterns of Sierra Nevada snowpack. SWE is used to determine the total water content for a given snow depth. It can be quantified by taking a given depth of snow and melting it; the resultant water content represents the SWE. This is useful since snow densities can fluctuate as a result of variations in snowfall as well as melt and ablation events in the snowpack. SCD represents the date of peak snowpack accumulation, which is useful in understanding snowmelt onset. SNOWC characterizes the total areal coverage of snow over a given region. This metric is helpful in quantifying shifts in regional and global albedo as well as the freezing-line extent in mountainous environments. Over the historical record, the Sierra Nevada has shown a mean difference in 1 April SWE of 2.2% (i.e., a northern Sierra Nevada decline of 50%–75% and a southern Sierra Nevada accumulation of 30%; Mote et al. 2005), western U.S. SCD was found to shift 0.7 days earlier per decade (Kapnick and Hall 2012), and total SNOWC declined by 9% across the Northern Hemisphere (Rupp et al. 2013). The shift in SCD appears to be 8 days earlier per degree Celsius of warming in temperatures associated with the end of winter season (March and April). In addition, Bales et al. (2006) found that the fraction of storms that occur with surface temperatures in the range from −3° to 0°C accounts for up to 36% of the annual precipitation events in many parts of the Sierra Nevada, highlighting the sensitivity of snow storms in the Sierra Nevada to increasing temperatures due to anthropogenic global climate change. Using IPCC Fifth Assessment Report RCP 4.5 and 8.5 scenarios, projected end-of-the-century trends for snowpack highlight that western U.S. SWE may decline by 40%–70% (Pierce and Cayan 2013), snowfall may decrease by 25%–40% (Pierce and Cayan 2013), more winter storms may tend toward rain rather than snow (Bales et al. 2006), and relatively warmer storms (e.g., ARs) may be more frequent and intense for California (Dettinger 2011). In a review paper by Gimeno et al. (2014), Dettinger et al. (2011) represented the only western-U.S.-specific paper on the future projected trends of ARs. Of note is that the authors expressed that the results in this study were a preliminary step and should be assessed more from a qualitative sense because of the small sample size of AR events in the CMIP5 archive and the various assumptions associated with the relatively coarser temporal and spatial extents of the models in the CMIP5 archive. Therefore, if the aforementioned projected outcomes hold, mean precipitation is not expected to change dramatically, but interannual variability will likely increase through modulation in AR events. Because snowpack is affected by both precipitation and temperature, it is expected that increased end-of-century temperatures

coupled with more intense warmer storms in the western United States will prevent snow accumulation and will lead to changes in runoff timing that could be problematic for water management. Thus, an analysis of causal mechanisms of snowpack accumulation and snowmelt timing, with a dynamic inclusion of large-scale atmosphere–ocean drivers and an accurate representation of the complex topography of California, is needed to allow water managers to make more informative and preemptive decisions on California's water future.

One key approach to address the aforementioned need is through climate models; however, both global and regional models have limitations in their predictive capacities. As demonstrated by the North American Regional Climate Change Assessment Program (NARCCAP), regional climate models (RCMs) were shown to produce too-dry, too-warm, and too-little-SWE conditions for the western United States, and snow-cover duration was found to start too late and to end too early (Salzmann and Mearns 2012). Model bias was associated with inadequate topography representation, imperfections in observational data, and differing land-surface model (LSM) components (Salzmann and Mearns 2012). Caldwell (2010) similarly found that RCMs generally overpredict winter precipitation in California, whereas GCMs generally underpredict winter precipitation in California. The precipitation bias associated with GCMs was related not solely to model resolution (this factor was standardized before comparison) but also to factors such as subgrid-scale parameterizations and coarse model topography (Caldwell 2010). The aforementioned RCM findings regarding precipitation and SWE appear contradictory to one another, but note that California hydroclimatic trends have shown dissimilarities from several of those shown in other parts of the western United States (Mote et al. 2005; Kapnick and Hall 2012), likely because of a combination of relatively higher topographical elevation in the southern Sierra Nevada (when compared with other western U.S. mountain ranges), proximity to the Pacific Ocean, and effects from ARs.

This paper aims to analyze the efficacy of variable-resolution modeling using the Community Earth System Model (VR-CESM) at resolutions of 0.125° (14 km) and 0.25° (28 km) in representing Sierra Nevada snowpack, in comparison with observational, reanalysis, and dynamically downscaled model results. Variable-resolution modeling is a novel tool for modeling the climate system and represents a hybrid of global and regional climate models. We envision that this new modeling framework will bring added value to the snowpack-modeling community with the benefit of a global solution that accounts for major teleconnections and regional high-resolution, better representation of winter storms and orographic forcings. This hypothesis has been corroborated for temperature and precipitation climatic trends within California (X. Huang et al. 2015, manuscript submitted to *J. Adv. Model. Earth Sys*.). These benefits will lead to a better representation of observed summary statistics for winter snowpack within a

GCM framework. Further, several studies have shown that CESM has skill in representing the major wintertime teleconnections of the western United States, including the ENSO (DeFlorio et al. 2013; Wang et al. 2014), the PDO (DeFlorio et al. 2013), and the PNA pattern (Li and Forest 2014). Teleconnection representation in these studies is expected to carry over into VR-CESM.

The structure of the remainder of the paper is as follows: Section 2 contains information about the CESM setup and experimental design, including VR-CESM grid implementation. Section 3 discusses the comparative datasets used to assess model efficacy. Section 4 provides summary statistical comparisons of snow trends on seasonal to multidecadal scales, including SWE and SNOWC. Section 5 provides further discussion and the conclusions of this study.

## 2. CESM setup and VR-CESM grid implementation

### *a. CESM setup*

This project utilized version 1.2 of CESM, a widely used and community-supported climate model developed by the National Center for Atmospheric Research (NCAR) and the U.S. Department of Energy. CESM is a fully coupled GCM composed of seven geophysical models that simulate the major components of the Earth system, including the atmosphere, land surface, land ice, ocean, ocean waves, river runoff, and sea ice, all of which can be coupled dynamically. One of the “F component” sets in CESM (“FAMIPC5”) is the standard protocol for the Atmospheric Model Intercomparison Project and was used for each of the CESM simulations in this study (Gates 1992). This component set consists solely of the atmosphere–land coupled model with prescribed sea surface temperatures (SSTs) and sea ice extent. This limited configuration maximizes computational efficiency and inhibits propagation of model bias. This is advantageous for a local server environment (<1000 processors per simulation) like the one used in this study. Although the oceanic and sea ice systems were not incorporated dynamically into this study, this component set ensures that interannual climate variability (mainly via SST anomalies) and global albedo effects from sea ice extent are incorporated into the simulations. Future research will target the VR-CESM simulation performance with and without a dynamic ocean model. Thus, for this study, only the atmosphere model [Community Atmosphere Model, version 5.3 (CAM5); Neale et al. 2010] and the LSM [Community Land Model, version 4.0 (CLM4.0), with satellite phenology (SP); Oleson et al. 2010] were utilized.

CAM was run with the spectral-element (SE) dynamical core with a cubed-sphere grid structure (Taylor et al. 1997; Dennis et al. 2011). CAM-SE uses a continuous Galerkin spectral finite-element method for solving the hydrostatic atmospheric primitive equations. CAM-SE provides several benefits over other CESM dynamical cores, including linear scalability with increasing computer processor counts, machine-precision conservation of

mass and tracers, elimination of nonuniform grid spacings due to convergence zones at higher latitudes, and variable-resolution capabilities (Taylor and Fournier 2010; Dennis et al. 2011; Zarzycki et al. 2014a,b; Zarzycki and Jablonowski 2014). The CAM5 physics is broken down into six main categories: shallow convection (Park and Bretherton 2009), deep convection (Neale et al. 2008), microphysics (Morrison and Gettelman 2008), macrophysics (Park et al. 2014), radiation (Iacono et al. 2008), and aerosols (Ghan et al. 2012). Details on each of the physics schemes can be found in Neale et al. (2010).

CLM subdivides each cell into land types such as glacier, lake, urban, vegetated, and wetland (Oleson et al. 2010; Lawrence et al. 2011). The vegetated component of the grid cell is further broken down into various soil types that are then characterized by 16 unique plant functional types (PFTs), including nonvegetated. CLM4.0 PFTs include five evergreen species and six deciduous species for temperate, boreal, and tropical climates, three grasses for Arctic and non-Arctic climates (with $C_3$ and $C_4$ variations), and a few staple cereal crops. PFT cover is derived from the Moderate Resolution Imaging Spectroradiometer (MODIS) satellite data at 0.5° resolution with canopy heights for each of the PFTs assumed to range from 0.5 m (crops, grasses, and shrubs) to 35 m (trees). PFTs and percent cover of PFTs within each vegetated land unit play a crucial role in shaping snowpack trends. This is because the interaction between the canopy and snowpack is PFT specific for biogeochemical, radiative, and hydrological processes such as interception, throughfall, canopy drip, water removal via transpiration, and optical-property interactions that are based on leaf angle and specific PFT (Lawrence et al. 2011).

The parameterizations of snowpack within CESM are based primarily on work done by Anderson (1976), Jordan (1991), and Yongjiu and Qingcun (1997). These parameterizations characterize several important state variables for snowpack, including the mass of water, mass of ice, snowpack-layer thickness, temperature profile of the snowpack layer, black carbon and mineral deposition, and snowpack aging and optical properties. The model is discretized using five snow layers with dynamic compaction, water transfer, and energy transfer.

*b. VR-CESM grid implementation*

The VR-CESM grids were generated using a freely available software package (“SQuadGen”; Ullrich 2014). To generate the variable-resolution grid files, SQuadGen interpolates a picture-image file, with variations in its grayscale properties, creates a refinement map, and uses spring dynamics to smooth the transitional regions between various grid resolutions. VR-CESM 0.25° (28-km resolution) and VR-CESM 0.125° (14-km resolution) grids were constructed for both CAM and CLM (Fig. 1). Topographic smoothing was varied between the two VR-CESM 0.25° simulations [VR-CESM 0.25° (smooth) and VR-CESM 0.25° (rough)] without modifying the grid structure

so as to assess the sensitivity of topographical influences on VR-CESM simulations. This study represents the first time that variable-resolution grids were implemented into CLM.

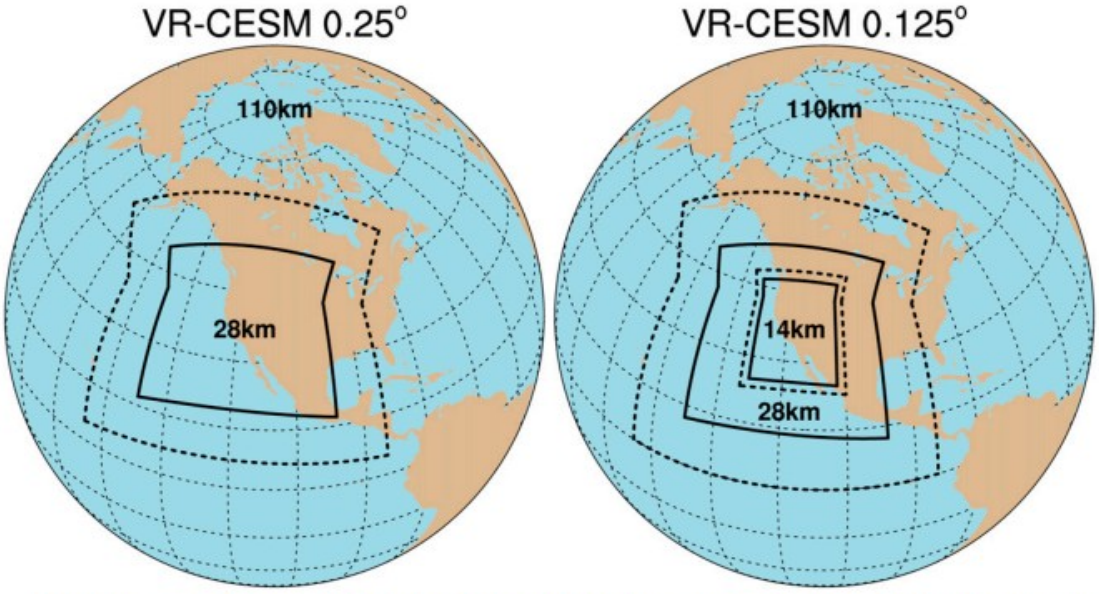


FIG. 1. The two variable-resolution GCM grids [(left) 0.25° (28 km) and (right) 0.125° (14 km)] used for this study. Both grids are developed on a cubed sphere with a 1.00° quasi-uniform resolution (111 km). The dashed lines highlight the model transition region, and the solid lines indicate the higher-resolution regions.

c. Topographic representation in the VR-CESM simulations

Topographical datasets were generated for each variable-resolution grid. The topographic smoothing was varied between the two VR-CESM 0.25° simulations by adjusting the c parameter from Eq. (1) in Zarzycki et al. (2015). In the case of the VR-CESM 0.25° (smooth) topography, this parameter was equal to 1.33 times that used for generating the VR-CESM 0.25° (rough) case. This resulted in the differences in topographical representation seen in Figs. 2a and 2b. Careful consideration is required when generating the VR-CESM topographical datasets because CAM-SE uses terrain-following vertical coordinates that exhibit, with excessive terrain roughness, a tendency toward generation of spurious vertical velocities and numerical artifacts (Zarzycki et al. 2015). The topographical datasets were derived using bilinear interpolation with a linear smoothing operator on the National Geophysical Data Center (NGDC) global-relief 2-minute gridded elevations/bathymetry for the world dataset (ETOPO2v2; NGDC 2006) coinciding with the variable-resolution grids' surface geopotential and the order of the hyperviscosity term. This provides more (less) topographical structure in the high-resolution (low resolution) region of the nest. For example, maximum Sierra Nevada topographical elevations (see Fig. 2) in the 111-, 28-, and 14-km resolutions of CESM were 1583.31, 2677.08, and 3147.28 m, respectively. When compared with the ETOPO2v2 NGDC dataset,

topographical elevation in the Sierra Nevada matches more closely as model resolution increases (Fig. 2).

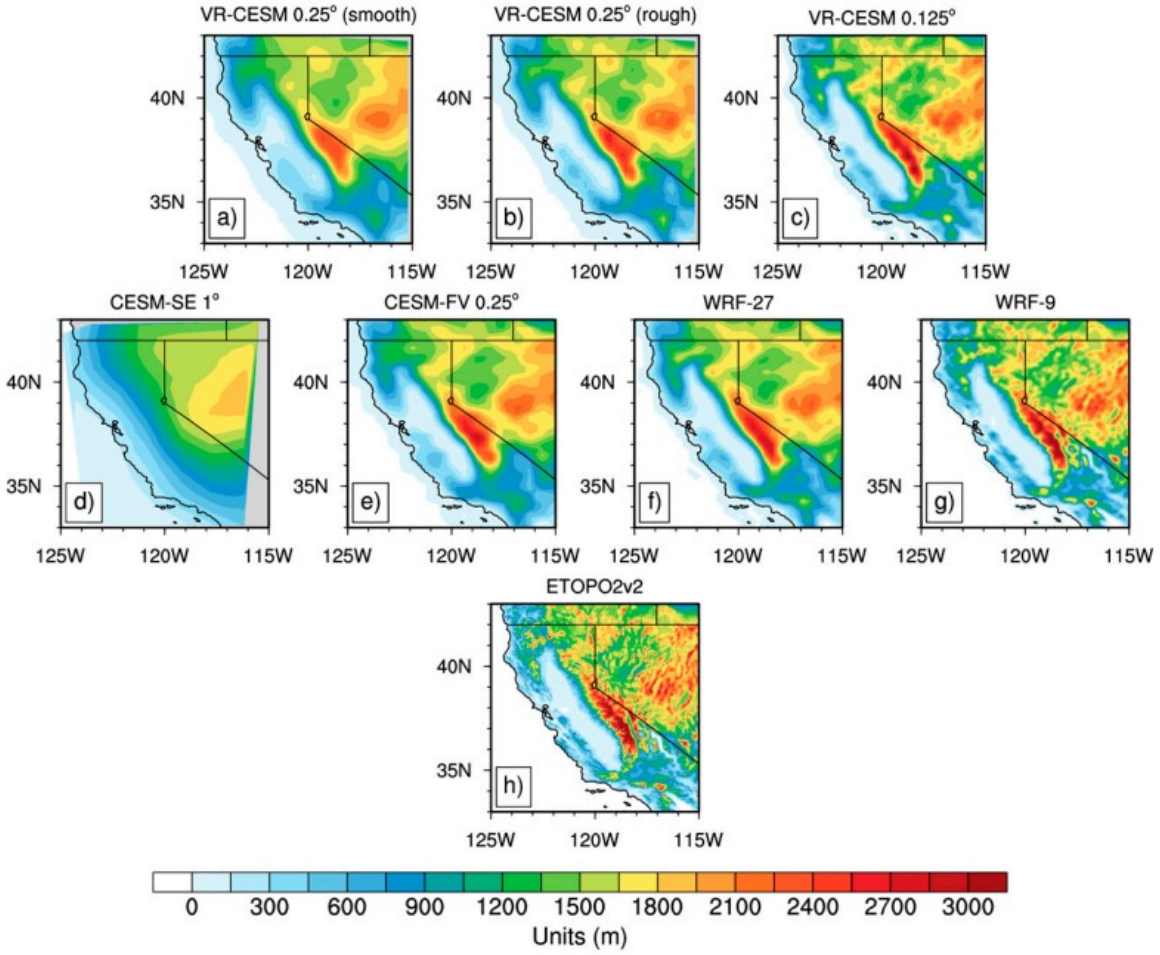


FIG. 2. Topographical representation of the Sierra Nevada and surrounding regions across model datasets. (a)–(c) Topography from variable-resolution CESM is displayed in order of increasing grid resolution. (d)–(g) The standard CESM and WRF simulations are displayed in order of increasing resolution. (h) The ETOPO2v2 dataset, representing 2-min (2 km) gridded topographic relief.

## 3. Reference datasets and statistical methods

### *a. Reference datasets*

Observational datasets for snowpack metrics such as SWE and SNOWC are particularly difficult to develop in mountainous environments. The fractal nature of snowpack deposits, quick shifts in elevation, angular differences in topography, alpine vegetation cover, cloud cover, and the large footprint radius associated with satellite instrumentation are key challenges. In addition, many satellite products span less than a decade, preventing analysis of climate patterns over decadal timeframes. In situ measurements help to alleviate some of the highlighted issues, yet they are irregularly located and so may not be representative in regions of rapidly varying topography. LSMs have been used to abate the discontinuous nature of in situ observations but often contain their own biases. Therefore, to provide a

rigorous assessment, a blend of the aforementioned data types will be used in this assessment.

The datasets that this study used for validation purposes are listed in Table 1. Datasets vary in snowpack-product availability (i.e., SWE and SNOWC), spatial and temporal resolution, map projection, and temporal range. Therefore, all datasets were standardized to monthly averaged, seasonally averaged (DJF), and climate-averaged (DJF from 1980 to 2005) temporal resolutions during the assessment of the VR-CESM simulations. To accomplish this task, utilities from the "netCDF" operators (NCO), the climate-data operators (CDO), and the NCAR Command Language (NCL) were used.

TABLE 1. Datasets and associated metadata used to analyze the accuracy of the VR-CESM simulations.

| Datasets | Snowpack product | Spatial resolution | Temporal resolution | Projection | Years assessed |
|---|---|---|---|---|---|
| VR-CESM 0.25° (smooth) | SWE and SNOWC | 28 km | Daily | VR-CESM in CAM and CLM—equidistant | 1980–2005 |
| VR-CESM 0.25° (rough) | SWE and SNOWC | 28 km | Daily | VR-CESM in CAM and CLM—equidistant | 1980–2005 |
| VR-CESM 0.125° | SWE and SNOWC | 14 km | Daily | VR-CESM in CAM and CLM—equidistant | 1980–2005 |
| Uniform CESM (SE and FV) | SWE and SNOWC | 111 km and 28 km | Daily | Equidistant | 1980–2005 |
| WRF | SWE and SNOWC | 27 km, 9 km | Daily | Lambert conformal | 1980–2005 |
| Daymet | SWE | 1 km | Daily | Lambert conformal conic | 1980–2005 |
| Cal-Adapt | SWE | 14 km | Monthly | Equidistant | 1980–2005 |
| SNOTEL | SWE | Point source (19 stations) | Daily | Point source (automated station) | 1980–2005 |
| NLDAS-2 | SWE and SNOWC | 14 km | Hourly, monthly | Equidistant | 1980–2005 |
| NCEP (CFSv2) | SWE and SNOWC | 35 km | Daily | Equidistant | 1980–2005 |
| NARR | SNOWC | 32 km | Daily | Lambert conformal | 1980–2005 |
| MODIS/*Terra* | SNOWC | 5 km | Monthly | Geographic lat/lon or climate modeling grid | 2000–13 |

The North America Land Data Assimilation System Phase 2 (NLDAS-2) produced 0.125° datasets by incorporating large quantities of observational and model reanalysis datasets into three non–atmosphere coupled LSMs (i.e., Princeton's implementation of VIC, NOAA's Noah, and NASA's Mosaic) over the continental United States. The three datasets provide SWE and SNOWC and are extensively analyzed by Xia et al. (2012a,b). For the 2008 California climate-change assessment, four GCM (i.e., CCSM3, CNRM, GFDL, and PCM1) datasets were downscaled using bias-corrected statistical downscaling methods along with the VIC model at a resolution of 0.125°. This dataset, known as Cal-Adapt, provides SWE values over the entirety of California, with the method discussed in Maurer and Hidalgo (2008). The "Daymet" dataset provides SWE estimations that are based on meteorological stations. The station data are then extrapolated, using a truncated Gaussian weighting filter, to create a high-resolution gridded output (Thornton et al. 2014). The MODIS satellite remote sensing dataset [MODIS/*Terra* Snow Cover Monthly 0.05° (5 km), version 5 (MOD10CM V005)] provides SNOWC using a snow-mapping algorithm with a normalized-difference snow index (NDSI; Hall et al.

2006). The NDSI is used to distinguish between snow and other features (such as cloud cover) by using visible and shortwave near-IR spectral bands. A comprehensive analysis and a validation of the MODIS dataset for a region of the Sierra Nevada were conducted in Hall and Riggs (2007). The Snowpack Telemetry (SNOTEL) in situ dataset is composed of 32 automated observational stations spread throughout the Sierra Nevada that measure SWE (Serreze et al. 1999). The areal extent of the SNOTEL stations ranges from 38.07° to 42.99° in latitude and from −120.79° to −119.23° in longitude, with an average elevation of 2343 m. Of the 32 stations, only 19 were utilized, because they spanned the entire 1980–2005 temporal range. The North American Regional Reanalysis (NARR) dataset provides monthly averaged SNOWC output variables using a high-resolution atmospheric model (the Eta Model) forced by a Regional Data Assimilation System (RDAS; Mesinger et al. 2006). The other reanalysis dataset that was used (NCEP CFSv2) is an updated version (2013) of its predecessor (2004) and provided SNOWC data (Saha et al. 2014). The NCEP dataset provides better representations of 2-m surface temperature, Madden–Julian oscillation (MJO), and SST forecasts while upgrading overall performance in seasonal-to-subseasonal forecasting results relative to its predecessor, and its use has been advised for decision makers in the water management and agricultural sectors (Saha et al. 2014).

A 0.25° (finite volume; CESM-FV) and a 1° (spectral element; CESM-SE) uniform-resolution CESM run were used for comparison with the VR-CESM simulations as well. The 0.25° simulation is described in Wehner et al. (2014), and the 1° simulation was performed by the research team with the same component set and dynamical core as were used in the VR-CESM simulations. The final datasets utilized for this assessment were a pair of simulations conducted at the University of California, Davis, using the Weather Research and Forecasting (WRF) Model, which has been used extensively for regional climate studies. Several common parameterization combinations (including different cumulus schemes and radiation schemes) were tested over a 1-yr simulation period and were compared with gridded observations. Those final options were chosen for climate applications that balance long-term reliability and computational cost, representing a typical RCM configuration. Subgrid parameterizations include the Kain–Fritsch cumulus scheme (Kain 2004), the WSM 6-class graupel microphysics scheme (Hong and Lim 2006), and the CAM shortwave and longwave radiation schemes (Collins et al. 2004). The simulations used a nested domain with a coarse resolution of 27 km (WRF-27) and a finer-resolution domain of 9 km (WRF-9) situated over the western United States (centered over the Sierra Nevada). The initial and boundary conditions and sea surface temperatures were all provided by ERA-Interim reanalysis data, which is a widely used and validated dataset for this kind of work (Dee et al. 2011). Both WRF domains provide SWE and SNOWC output variables via the Noah LSM (Chen and

Dudhia 2001) coupled with the Yonsei University boundary layer scheme (Hong et al. 2006).

The Noah and CLM4.0-SP LSMs are derived from similar snow-model formulations (i.e., Anderson 1976) yet also deviate in several ways. The Noah LSM pulls primarily from Yen (1965), whereas CLM4.0-SP draws from Jordan (1991). This creates differences in both of the snow models' fundamental equations and parameterizations. Differences include number of snow layers (Noah LSM has three, whereas CLM4.0-SP has five), snow thermal conductivity (CLM4.0-SP uses a snow-density function and Noah LSM uses a constant), snow-cover hyperbolic functions (CLM4.0-SP utilizes a slightly more complicated formulation) and snowpack–canopy interactions (Oleson et al. 2010; Yang et al. 2011). Of relevance to this paper's overall conclusions is that snow depths (and thus SWE) estimations in the Noah LSM have been noted to be significantly overestimated in certain cases because of the assumption that snowpack density, physical characteristics, and thermal conductivity are constant, therefore neglecting heat transfers via meltwater movement in the snowpack (Yang et al. 2011).

*b. Statistical methods*

The DJF climatological mean state and seasonal variability in snow products found within the Sierra Nevada were analyzed. The assessment aimed to understand the efficacy of the new VR-CESM approach in representing snowpack trends against observation, reanalysis, and other widely used GCMs and RCMs. To do this, the datasets were remapped to similar map projections and resolutions using both the Earth System Modeling Framework capabilities in the NCL and the "TempestRemap" (Ullrich and Taylor 2015) software suite. The observational and reanalysis datasets were further remapped to all possible resolutions used in the models (i.e., 0.125°, 0.25°, and 1°). The climate averages and seasonal averages were computed using a mask of the Sierra Nevada (see Fig. 3). This mask was developed by the U.S. Environmental Protection Agency (EPA) ecoregions classification system (ecoregion level III—6.2.12). Summary statistics of the Sierra Nevada were calculated for each of the datasets for SWE and SNOWC, including mean, standard deviation, lower quartile, median, upper quartile, and maximum.

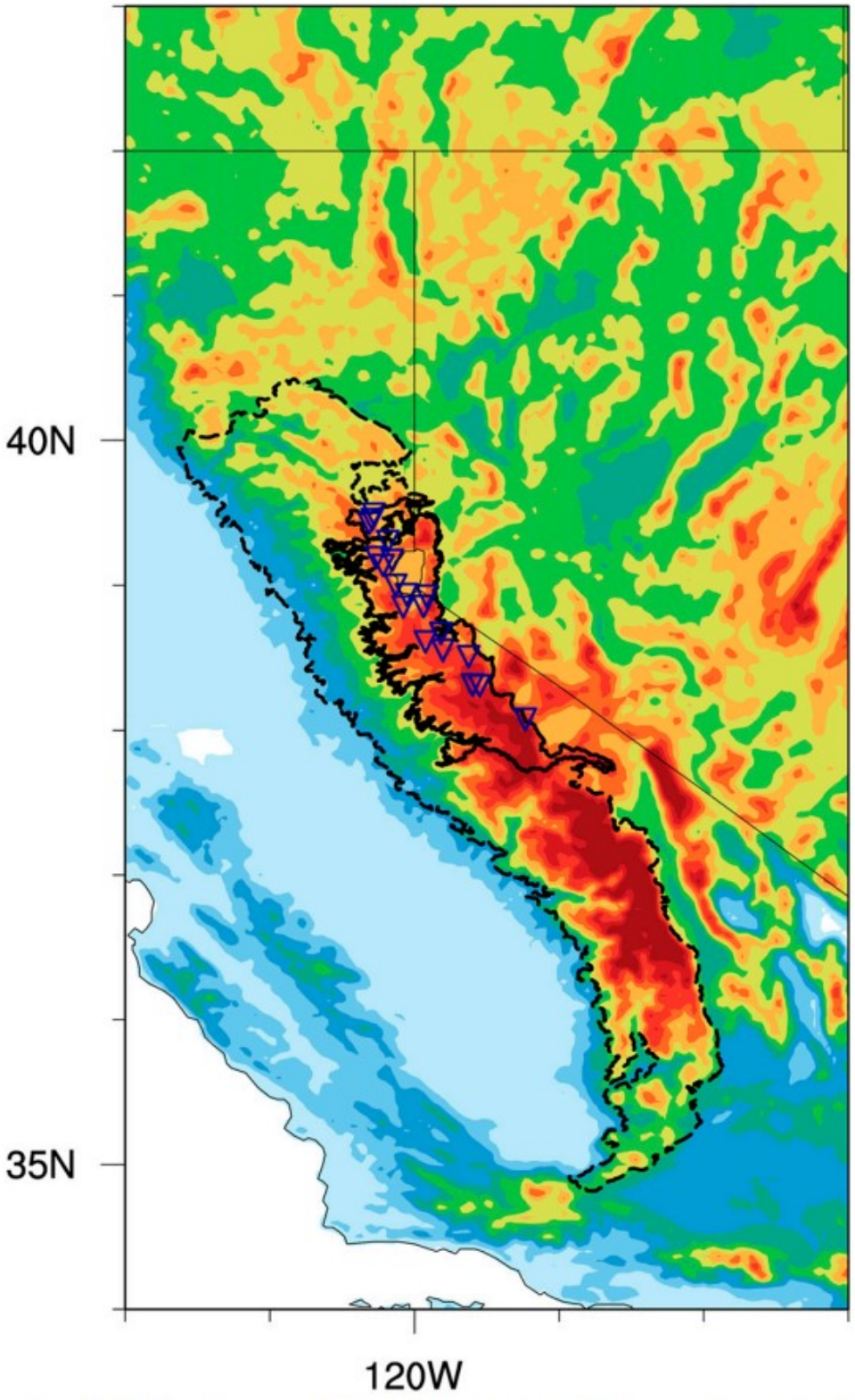


FIG. 3. The EPA ecoregion level-III (6.2.12) shapefile mask used for summary statistic calculations of the Sierra Nevada (dashed black outline). SNOTEL station locations (blue triangles) are overlaid onto the ETOPO2v2 topography. The solid black outline is used to indicate the subregion used to compare model and reanalysis data with SNOTEL stations.

For most of the datasets assessed, 25 seasons of average DJF values were used. WRF-9 had 22 DJF seasons. In addition, MODIS had 12 DJF seasons, many of which fall outside the historical period (1980–2005 vs 2000–12), but, because of the scope of this paper in analyzing the climatological and seasonal mean trends (rather than precise seasonal forecasting), this was assumed to be largely irrelevant.

## 4. Seasonal and multidecadal snow trends in the Sierra Nevada

### *a. Snow water equivalent summary statistics*

A panel plot of the DJF average SWE is shown across datasets for California (Fig. 4). Clear resolution dependence is apparent across all modeling platforms. Each of the datasets highlighted an overall increasing trend in SWE with an increase in model resolution, likely correlated with topographical representation (see Fig. 2) and resultant orographic forcing on weather fronts as well as sustained below-freezing temperatures. Of note is that the NCEP dataset did not characterize enough SWE for the Sierra Nevada region to be further assessed in greater statistical detail. The model datasets are compared with the average of the reanalysis datasets at their closest respective resolution of 0.125°, 0.25°, or 1°. Within the Sierra Nevada masked region, VR-CESM 0.125° and VR-CESM 0.25° (rough) demonstrated the closest statistical match across all observational and reanalysis datasets, with mean DJF SWE absolute-bias values of 6.4 and 2.7 mm, respectively (the reanalysis-dataset average SWE value was 97.4 mm), and median values within 8–13 mm (Table 2). Maximum DJF SWE values were most closely represented by CESM-FV 0.25° and VR-CESM 0.25° (rough), both within 68 mm. Note that an artificial cap on maximum SWE at 1000 mm is imposed in CLM4.0, which affected maximum SWE values for all VR-CESM and uniform CESM simulations. CESM-FV 0.25° and WRF-9 both showed a positive bias in DJF SWE values for mean and median when compared with the reanalysis-dataset average. CESM-FV 0.25° had a positive bias of 1.8 times the mean DJF SWE and 2.4 times the median value for the Sierra Nevada mask. WRF-9 exhibited a similar response, with a positive bias of 2.4 times the mean and 1.4 times the median DJF SWE. The coarser-resolution version of VR-CESM and WRF had a negative bias with VR-CESM 0.25° (smooth) at one-half the mean for DJF SWE in the Sierra Nevada and WRF-27 at 74%. CESM-SE 1°, the model resolution used in most IPCC simulations, was unable to represent both climatological and seasonal DJF SWE trends in the Sierra Nevada, with a maximum DJF SWE value of 41.7 mm (<5% of the reanalysis-dataset average maximum value), with similar tendencies seen in the mean and median values as well.

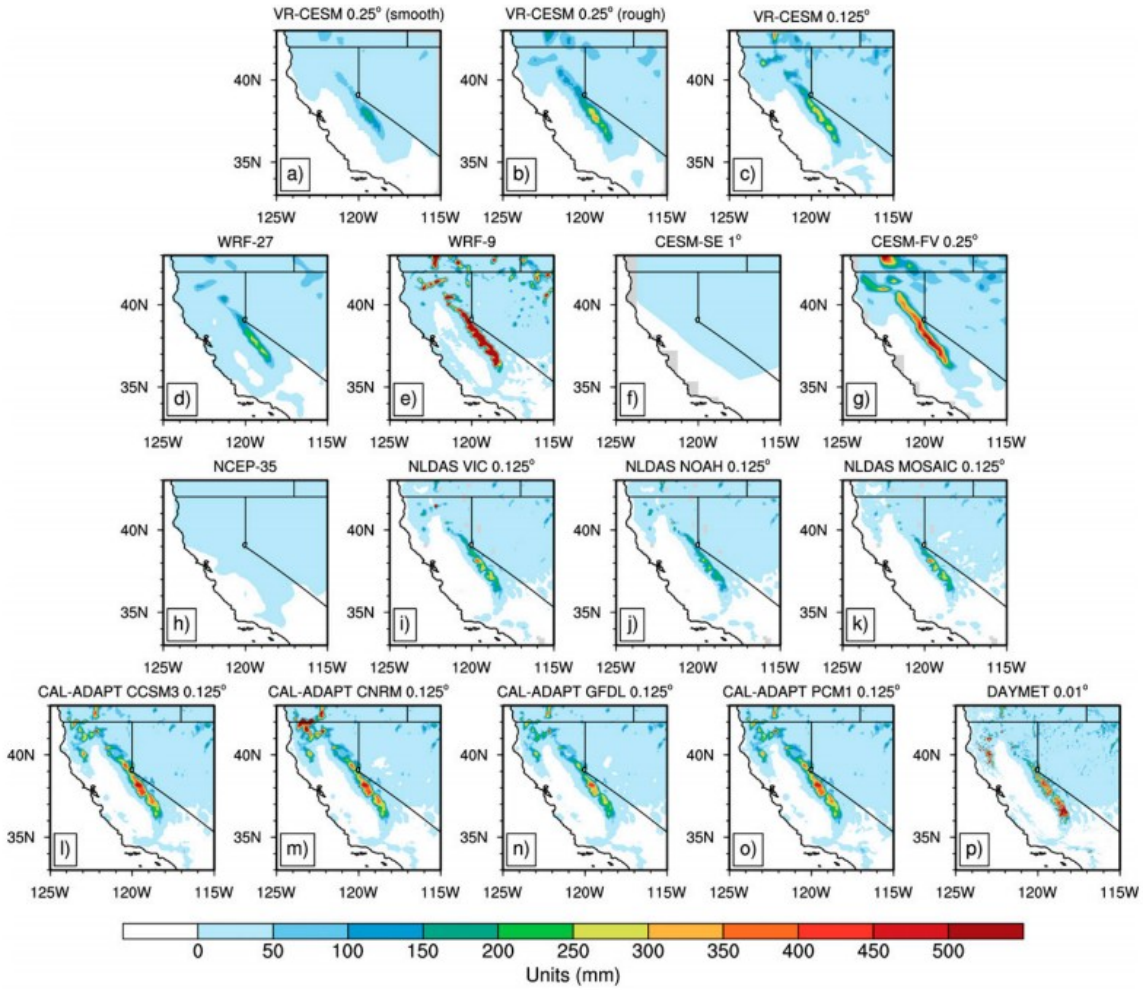


FIG. 4. Average climatological DJF SWE across model and observational datasets over California.

TABLE 2. Summary statistics of seasonally averaged SWE in the Sierra Nevada.

| Model | DJF seasons | Mean | Std dev | Lower quartile | Median | Upper quartile | Max | Sierra Nevada mask points |
|---|---|---|---|---|---|---|---|---|
| VR-CESM 0.25° (smooth) | 25 | 50.4 | 80.1 | 3.10 | 19.8 | 60.9 | 663 | 2175 |
| VR-CESM 0.25° (rough) | 25 | 95.2 | 134 | 5.30 | 32.9 | 132 | 750 | 2175 |
| VR-CESM 0.125° | 25 | 91.0 | 125 | 7.40 | 37.6 | 125 | 751 | 8775 |
| WRF-27 | 25 | 71.6 | 102 | 6.20 | 29.2 | 91.0 | 701 | 2175 |
| WRF-9 | 22 | 233 | 365 | 5.60 | 48.8 | 314 | 3090 | 14 058 |
| WRF-9 (regrid 0.125°) | 22 | 231 | 349 | 7.60 | 63.2 | 317 | 2850 | 7721 |
| CESM-SE 1° | 25 | 3.40 | 7.50 | 0.00 | 0.50 | 2.40 | 41.7 | 150 |
| CESM-FV 0.25° | 25 | 179 | 188 | 23.6 | 111 | 291 | 875 | 2175 |
| Daymet | 25 | 109 | 176 | 1.40 | 36.9 | 141 | 1000 | 1 202 620 |
| Daymet (regrid 0.125°) | 25 | 107 | 173 | 1.60 | 35.1 | 140 | 1000 | 8678 |
| Daymet (regrid 0.25°) | 25 | 102.3 | 168.4 | 1.90 | 32.0 | 127 | 1000 | 2156 |
| Daymet (regrid 1°) | 25 | 28.0 | 36.8 | 2.00 | 12.1 | 39.8 | 174 | 149 |
| NLDAS VIC 0.125° | 25 | 72.9 | 103 | 2.90 | 29.1 | 101 | 777 | 8748 |
| NLDAS VIC (regrid 0.25°) | 25 | 73.8 | 102 | 3.10 | 29.4 | 105 | 629 | 2169 |
| NLDAS VIC (regrid 1.00°) | 25 | 38.1 | 71.3 | 1.50 | 7.80 | 30.8 | 345 | 149 |
| NLDAS Noah 0.125° | 25 | 56.3 | 84.2 | 1.50 | 19.7 | 75.5 | 616 | 8775 |
| NLDAS Noah (regrid 0.25°) | 25 | 57.4 | 84.4 | 1.70 | 21.1 | 75.9 | 518 | 2175 |
| NLDAS Noah (regrid 1°) | 25 | 28.7 | 56.4 | 0.70 | 5.60 | 23.0 | 321 | 150 |
| NLDAS Mosaic 0.125° | 25 | 59.5 | 98.6 | 0.60 | 11.3 | 76.3 | 773 | 8748 |
| NLDAS Mosaic (regrid 0.25°) | 25 | 60.5 | 98.2 | 0.70 | 11.6 | 79.2 | 647 | 2171 |
| NLDAS Mosaic (regrid 1°) | 25 | 27.1 | 60.9 | 0.19 | 2.40 | 14.2 | 325 | 149 |
| Cal-Adapt CCSM3 0.125° | 25 | 134 | 154 | 9.60 | 80.7 | 202 | 1060 | 8775 |
| Cal-Adapt CCSM3 (regrid 0.25°) | 25 | 136 | 155 | 9.90 | 80.8 | 206 | 944 | 2175 |
| Cal-Adapt CCSM3 (regrid 1°) | 25 | 73.4 | 88.1 | 1.20 | 48.4 | 107 | 416 | 150 |
| Cal-Adapt CNRM 0.125° | 25 | 125 | 157 | 8.10 | 67.3 | 185 | 1210 | 8773 |
| Cal-Adapt CNRM (regrid 0.25°) | 25 | 127 | 158 | 8.60 | 68.5 | 191 | 1090 | 2174 |
| Cal-Adapt CNRM (regrid 1°) | 25 | 66.4 | 88.2 | 2.40 | 27.4 | 89.8 | 544 | 149 |
| Cal-Adapt GFDL 0.125° | 25 | 95.0 | 121 | 5.40 | 49.1 | 141 | 959 | 8775 |
| Cal-Adapt GFDL (regrid 0.25°) | 25 | 96.3 | 122 | 5.60 | 49.3 | 141 | 855 | 2175 |
| Cal-Adapt GFDL (regrid 1°) | 25 | 47.0 | 65.2 | 1.90 | 26.0 | 67.6 | 448 | 150 |
| Cal-Adapt PCM1 0.125° | 25 | 129 | 151 | 14.2 | 75.2 | 186 | 926 | 8775 |
| Cal-Adapt PCM1 (regrid 0.25°) | 25 | 131 | 153 | 15.4 | 75.8 | 188 | 861 | 2175 |
| Cal-Adapt PCM1 (regrid 1°) | 25 | 73.8 | 90.5 | 6.60 | 45.4 | 99.1 | 426 | 150 |
| Reanalysis-dataset avg 0.125° | — | 97.4 | 134 | 5.50 | 45.9 | 138 | 915 | — |
| Reanalysis-dataset avg 0.25° | — | 97.9 | 134 | 5.90 | 46.1 | 139 | 818 | — |
| SNOTEL | 25 | 237 | 186 | 103 | 195 | 308 | 1220 | 19 stations |

b. Seasonal variability in snow water equivalent

SWE DJF mean seasonal variability is represented with a plot of standard deviation at each grid point across all datasets (Fig. 5). Characterization of interseasonal variability, in comparison with the reanalysis datasets, was shown to be more difficult for most of the modeling platforms. VR-CESM simulations were best represented by VR-CESM 0.25° (rough), which exhibited a slight positive bias of 1% relative to the reanalysis-dataset average (Table 2). VR-CESM 0.125° and VR-CESM 0.25° (smooth) were at 87% and 36% of the standard deviation, respectively. CESM-FV 0.25° had a large discrepancy in standard-deviation tendency with a positive bias of 2 times the reanalysis-dataset average of the reanalysis datasets. WRF-9 showed an exceedingly high variability with 6.8 times the standard deviation of the reanalysis-dataset average, although this could be partially amplified by the fact that Daymet and CESM SWE values were capped at 1000 mm. Although the standard-deviation values were highly variable across modeling platforms in comparison with the reanalysis-dataset average, the average seasonal interquartile ranges (IQR) were more closely aligned (Fig. 6). The

IQRs for VR-CESM 0.125° and VR-CESM 0.25° (rough) were closest to the reanalysis-dataset average, with a slightly negative bias of 11 and 7.8 mm, respectively. WRF-9 and CESM-FV 0.25° had a positive bias in IQR, with exceedingly high 75th percentiles, whereas VR-CESM 0.25° (smooth) and WRF-27 were conservative in their higher-quartile marks.

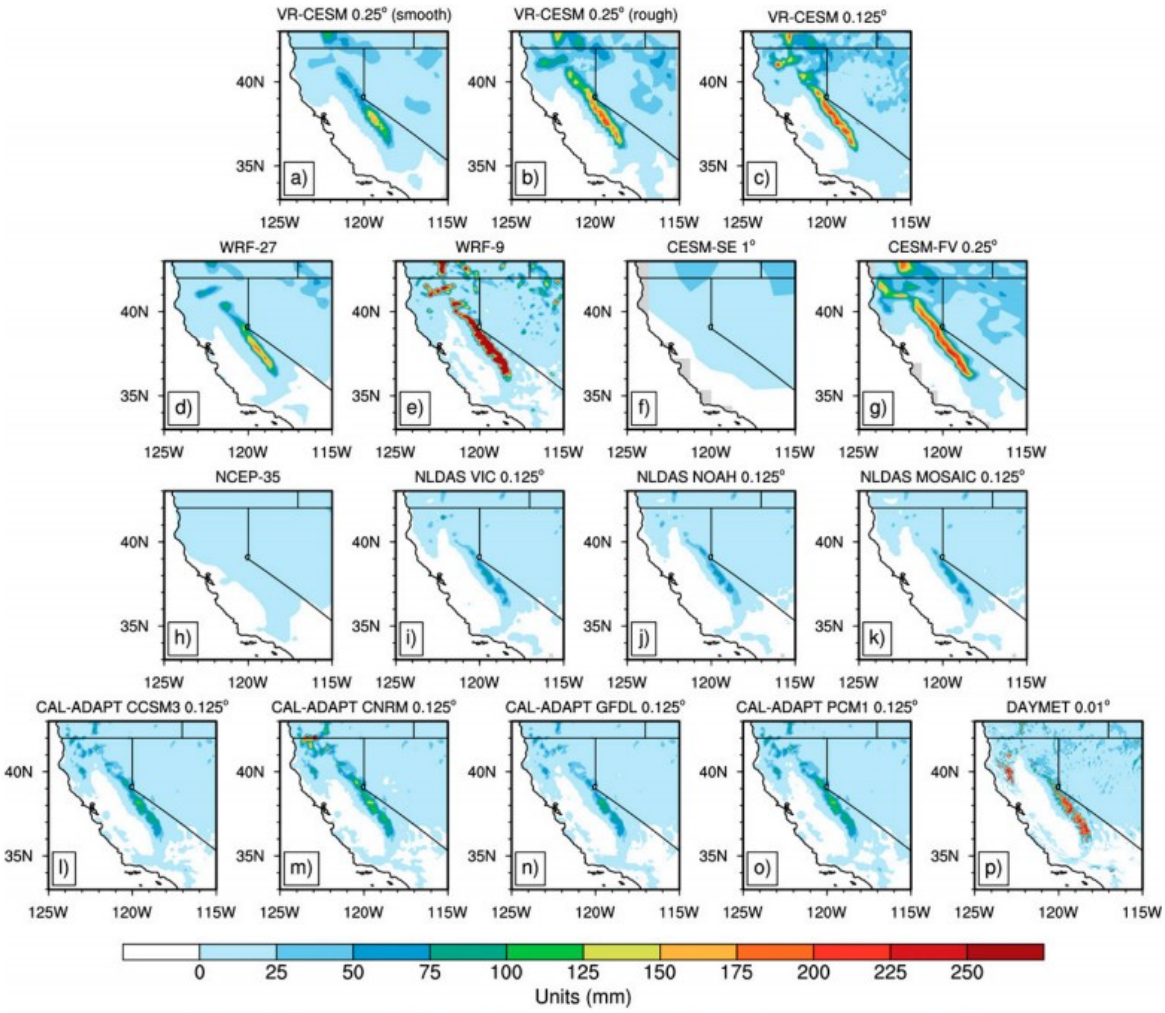


FIG. 5. As in Fig. 4, but for DJF variability (interannual std dev of the seasonal mean) of SWE.

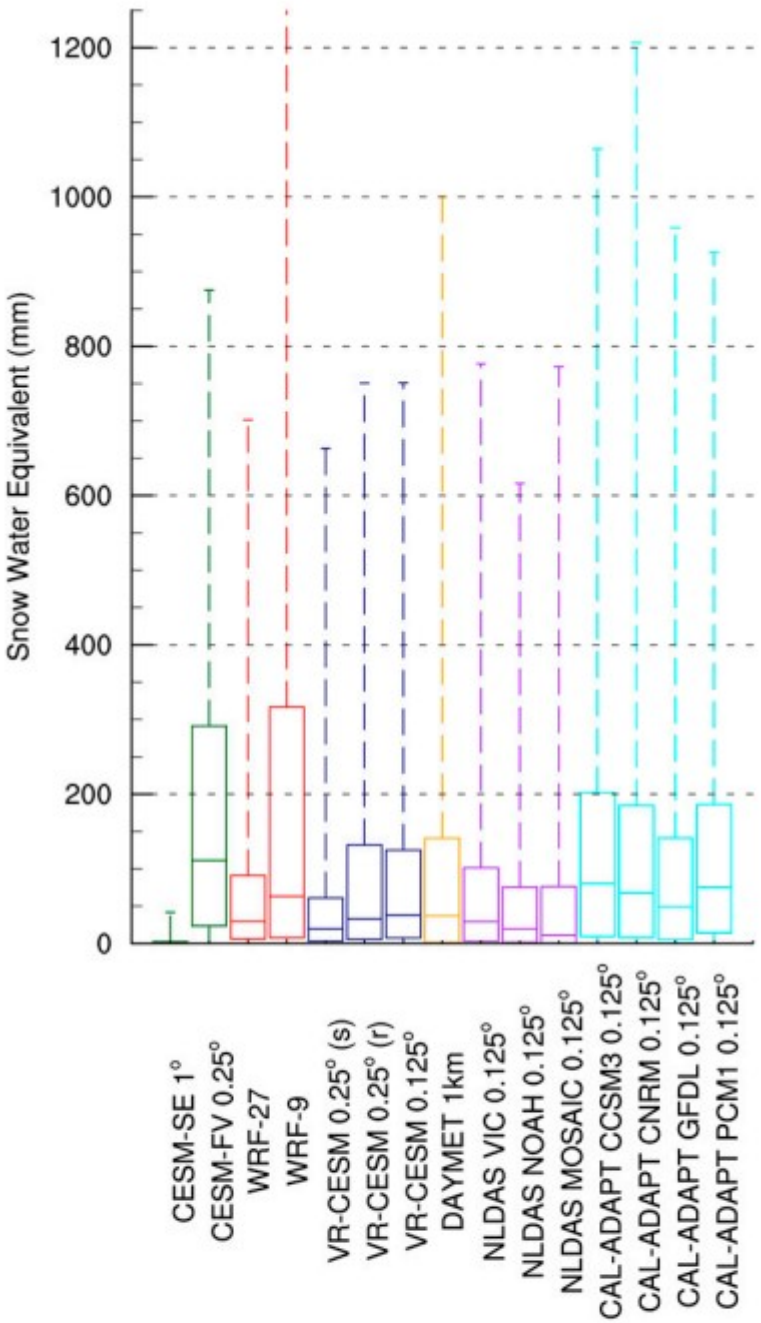


FIG. 6. Box plots of seasonal (DJF) Sierra Nevada SWE across modeling platforms and observational datasets. The box bottoms and tops represent the 25th- and 75th-percentile values within the Sierra Nevada masked region, with the median value indicated as the line inside the box. The range from minimum to maximum is depicted by vertically dashed lines. Regridding of reanalysis datasets to 0.25° (or 0.125° for Daymet) had no noticeable effect on the statistics and so is not shown.

c. Pattern correlation and bias in snow water equivalent

The average DJF centered Pearson product-moment coefficients, or the average statistical similarity between two datasets at identical locations for SWE across the 25 seasons (with removal of the mean), for all of the simulations were computed against each of the remapped reference datasets for the Sierra Nevada masked region (Table 3). The Pearson product-moment coefficients are calculated by computing the covariance of the two datasets and dividing by the product of their standard deviations. Averaging all of the Pearson product-moment coefficients across all grid points within the mask is useful in showing the seasonal similarity in SWE trend across the entire Sierra Nevada. Of interest is that the VR-CESM simulations were almost identical in average seasonal correlation with the reanalysis datasets (at ~0.67–0.71) for the Sierra Nevada. WRF-9, remapped to 0.125° (14 km) resolution, showed the highest seasonal correlation at 0.83; this was not unexpected given that the WRF simulations were forced by ERA-Interim data. Both CESM-FV 0.25° and CESM-SE 1° had the lowest correlations, with 0.28 and 0.19, respectively.

TABLE 3. SWE climatological bias and DJF seasonal Pearson product-moment coefficients (centered) within the Sierra Nevada. Absolute-value averages are computed to eliminate sign dependency in bias comparisons across datasets.

| Model | VR-CESM 0.125° | VR-CESM 0.25° (rough) | VR-CESM 0.25° (smooth) | WRF-9 | WRF-27 | CESM-FV 0.25° | CESM-SE 1° |
|---|---|---|---|---|---|---|---|
| | | | DJF climate bias (mm) | | | | |
| NLDAS VIC | 18.1 | 21.4 | 23.4 | 158 | 2.20 | 106 | 34.7 |
| NLDAS Noah | 34.7 | 37.8 | 7.00 | 175 | 14.2 | 122 | 25.3 |
| NLDAS Mosaic | 31.5 | 34.7 | 10.1 | 172 | 11.1 | 119 | 23.7 |
| Cal-Adapt CCSM3 | 42.8 | 40.3 | 85.1 | 97.3 | 63.9 | 43.9 | 70.0 |
| Cal-Adapt CNRM | 34.4 | 31.8 | 76.6 | 105.7 | 55.4 | 52.4 | 63.0 |
| Cal-Adapt GFDL | 4.00 | 1.10 | 45.9 | 136 | 24.7 | 83.1 | 43.6 |
| Cal-Adapt PCM1 | 37.9 | 35.3 | 80.1 | 102 | 58.9 | 48.9 | 70.4 |
| Daymet | 16.3 | 7.10 | 51.9 | 124 | 30.7 | 77.1 | 24.6 |
| Reanalysis-dataset absolute-value avg | 27.5 | 26.2 | 47.5 | 134 | 33.8 | 81.3 | 44.5 |
| | | | DJF Pearson pattern correlation | | | | |
| NLDAS VIC | 0.72 | 0.75 | 0.72 | 0.90 | 0.78 | 0.33 | 0.09 |
| NLDAS Noah | 0.69 | 0.71 | 0.68 | 0.88 | 0.74 | 0.35 | 0.07 |
| NLDAS Mosaic | 0.68 | 0.73 | 0.69 | 0.86 | 0.73 | 0.25 | 0.06 |
| Cal-Adapt CCSM3 | 0.71 | 0.75 | 0.75 | 0.85 | 0.75 | 0.32 | 0.32 |
| Cal-Adapt CNRM | 0.71 | 0.75 | 0.73 | 0.85 | 0.75 | 0.31 | 0.29 |
| Cal-Adapt GFDL | 0.70 | 0.74 | 0.75 | 0.84 | 0.73 | 0.29 | 0.32 |
| Cal-Adapt PCM1 | 0.72 | 0.76 | 0.73 | 0.86 | 0.76 | 0.35 | 0.33 |
| Daymet | 0.45 | 0.48 | 0.42 | 0.63 | 0.48 | 0.04 | 0.08 |
| Reanalysis-dataset avg | 0.67 | 0.71 | 0.68 | 0.83 | 0.71 | 0.28 | 0.19 |

In addition, seasonal average bias was computed across model simulations for the Sierra Nevada (Table 3). VR-CESM 0.25° (rough) had the smallest average seasonal bias to the reanalysis-dataset average with a slight negative bias of −2.7 mm, with VR-CESM 0.125° the next closest at −6.4 mm. WRF-9 showed the best agreement with the NLDAS reanalysis datasets. The WRF and uniform-CESM simulations had similar tendencies to one another, with a positive seasonal bias occurring in the higher-resolution simulations and a negative trend in the coarser-resolution simulations, much the same as Caldwell (2010) indicated for winter-precipitation tendencies in California. Figure 7 shows the average climatological difference in snow

water equivalent between model and reanalysis datasets. Bluer (redder) colors represent a more positive (negative) model bias over the simulation period. In general, higher-resolution models tend to overproduce SWE whereas lower-resolution models tend to underproduce SWE. This is likely due to the underrepresentation of topography within the model simulations. Of interest is that in several of the simulations a positive bias appears on the western slopes of the Sierra Nevada and a negative bias occurs on the eastern slopes. This may be caused by an oversensitivity to orographically forced upslope winds that push the model to overproduce snowfall as the storms move from the windward side to the leeward side of the Sierra Nevada. In addition, increased topographic height that does not preserve the fractal peaks and valleys in more detailed representations (see ETOPO2v2 in Fig. 2) could artificially enhance orographic uplift. For example, in Fig. 7 the orographic uplift bias was shown in the northern Sierra Nevada for VR-CESM 0.125° and less so in VR-CESM 0.25° (rough), a potential reason why nominal improvement was seen in snowpack characteristics for the Sierra Nevada when VR-CESM model resolution was increased.

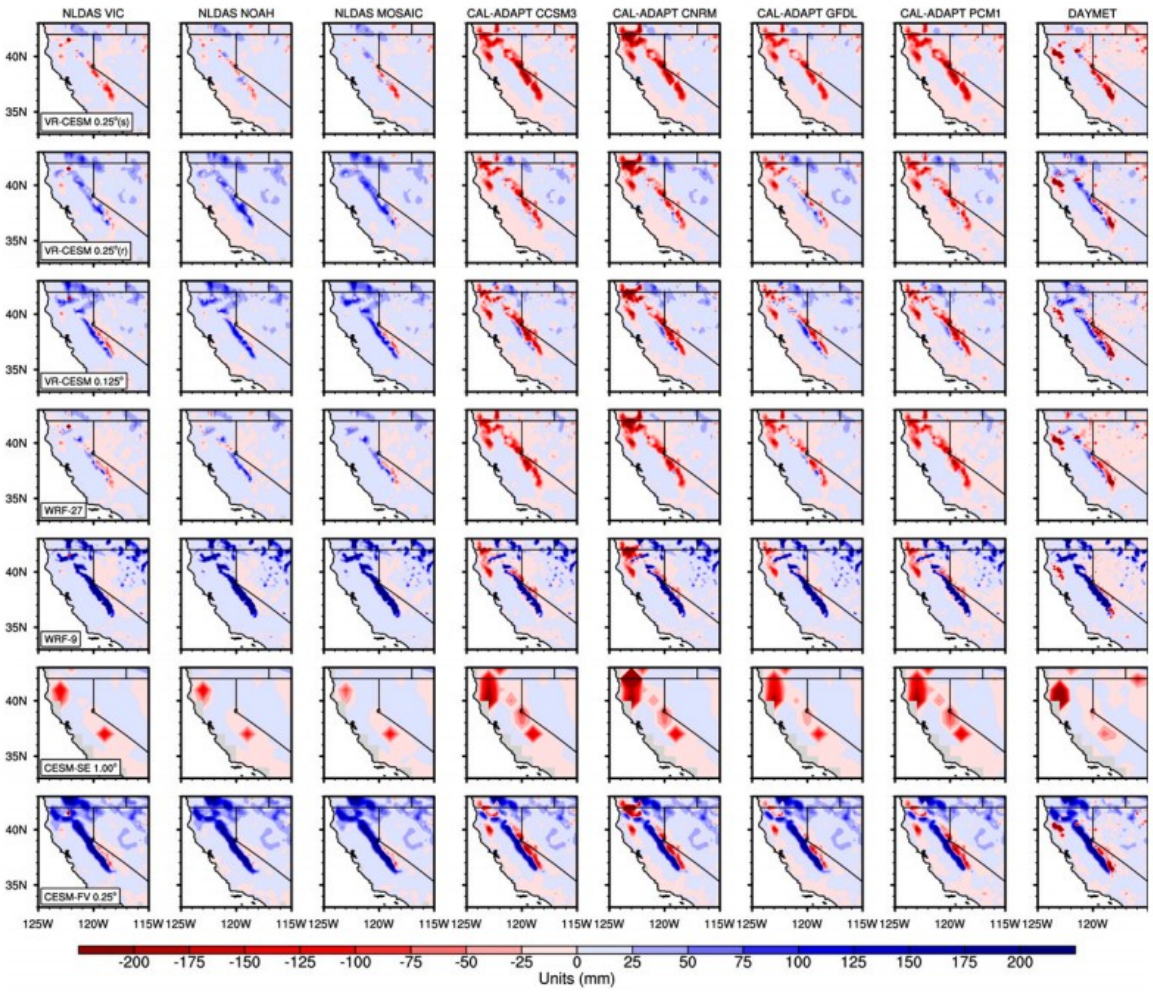


FIG. 7. Average difference in DJF SWE between model and reanalysis datasets over California. Rows indicate model output, and columns represent gridded or reanalysis datasets. Blue (red) indicates a model positive (negative) difference in SWE relative to the given reanalysis dataset.

d. Climatological behavior of total snowpack over the water year

The mean daily climatological total SWE (kg) within the Sierra Nevada was calculated to characterize the total water content of the region provided by snowpack (Fig. 8). By averaging the total SWE each day over all years (1980–2005) and then multiplying by the area of the mask (53 102 699 313 $m^2$), the average snowpack mass is shown for the Sierra Nevada across model and reference datasets. Each of the datasets was grouped according to its comparable-resolution counterparts [i.e., 1) 0.125° (14 km), 2) 0.25° (28 km), and 3) 1° (111 km)] to better showcase relative magnitudes of Sierra Nevada SWE found within a given climatological day. Note that Daymet has biases introduced during the dataset formulation that affect its overall ability to characterize midseason snowpack and thus alter the SCD and timing of snowmelt. Further, the Cal-Adapt datasets were not used because daily-resolution outputs were not available (only monthly and annual), and the first hour (0000) of each day within the NLDAS datasets was used within the

analysis. In general, VR-CESM 0.125° and VR-CESM 0.25° (rough) appear to match most closely to all of the reanalysis datasets in relative magnitude (Fig. 8). A bimodal profile in VR-CESM 0.125° is likely indicative of the artificial 1000-mm cap in SWE imposed within CLM4.0 to prevent excessive snow accumulation over Antarctica—future simulations will attempt to alleviate this by removing the cap away from the polar regions. WRF-9, remapped to 14 km, had a high bias associated with total SWE in the Sierra Nevada, with an SCD value of ~$21.4 \times 10^{12}$ kg (more than 2 times the value shown in most of the reanalysis datasets as well as VR-CESM 0.125°). In the 28-km datasets, the magnitude of total SWE is consistent with the 14-km results. VR-CESM 0.25° (rough) matched most closely to the NLDAS VIC 0.25° reanalysis dataset at $8.0 \times 10^{12}$ kg, with all other datasets falling under that mark ($<6.0 \times 10^{12}$ kg). The 111-km-resolution datasets differed greatly from one another, with the peak accumulation of CESM-SE 1° values falling much further below the remapped reanalysis datasets. This result further highlights the inability of standard-practice 1° GCM simulations to capture Sierra Nevada snowpack characteristics, especially with respect to total water content.

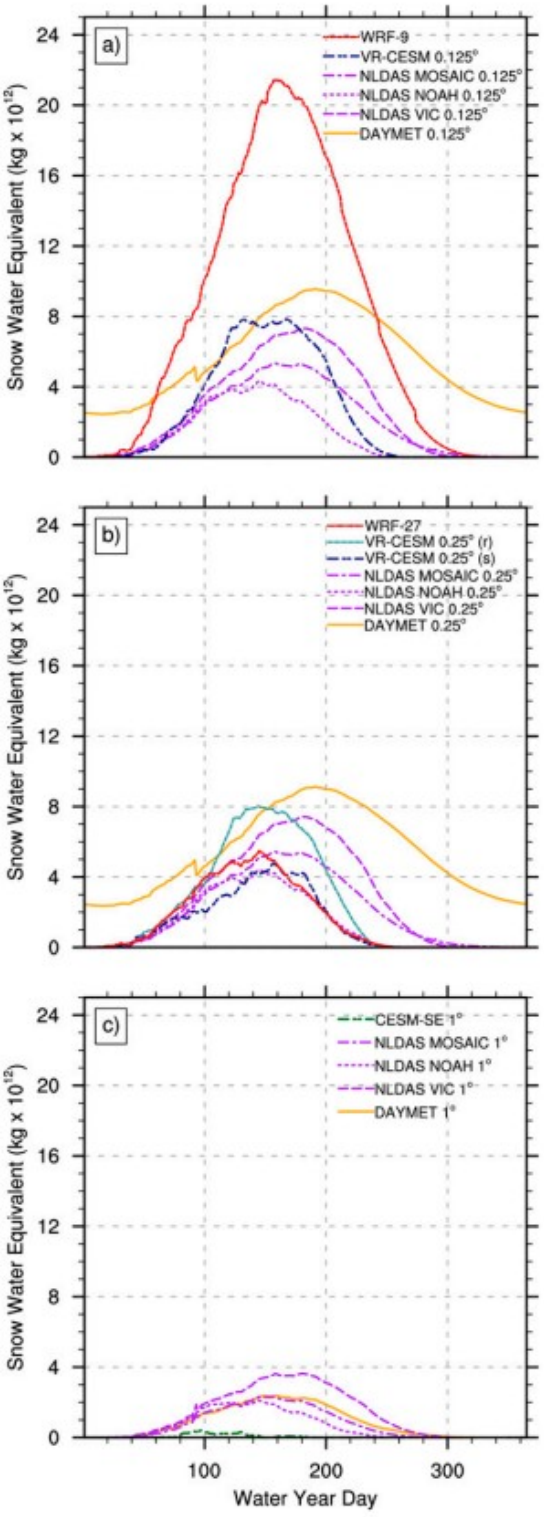


FIG. 8. Average water-yearday totals for SWE within the Sierra Nevada SNOTEL subregion. Plots are sorted according to the resolution of the models: (a) 0.125° (14 km), (b) 0.25° (28 km), and (c) 1° (111 km). The horizontal axis represents water yearday (from 1 Oct through 31 Sep).

e. Snowpack timing and melting patterns

Peak timing of western U.S. snowpack accumulation (or SCD) is traditionally thought to occur around 1 April (water day 182), although this has shifted because of regional warming trends in the western United States (Kapnick and Hall 2012; Montoya et al. 2014). Since most of the reanalysis datasets had discrepancies in representing the total water content and SCD within the Sierra Nevada, normalized values of average climate day SWE are shown in Fig. 9 for all datasets in comparison with 19 SNOTEL stations (Fig. 3). These stations were chosen on the basis of daily observation availability spanning 1980–2005. Further, the SNOTEL locations are representative of several elevations found within the Sierra Nevada, spanning from 1864 m (Spratt Creek) to 2879 m (Virginia Lakes Ridge). Of note is that the SNOTEL stations are clustered from the northern to central Sierra Nevada, with no stations present in the south. As such, a subregion of the Sierra Nevada was made to compare model results with observations from SNOTEL stations (see the solid black subregion in Fig. 3). This subregion was created using 12 of the USGS hydrologic units in the Sierra Nevada (Seaber et al. 1987). If a SNOTEL station was located within or near an adjoining hydrologic unit then the entire unit was kept (within the boundary of the Sierra Nevada ecoregion). Further, since the lowest-elevation SNOTEL station was located at 1864 m (Spratt Creek), a topographical threshold of 1824 m was imposed to create the subregion (this altitude was chosen to provide a buffer around Spratt Creek). The normalizations were computed by removing the relative mean from all climatological days within a given dataset and then dividing the resultant values by the standard deviation. Like the plots for the mean daily climatological sums of SWE, all datasets are grouped according to resolution, with added comparison with SNOTEL in each plot (Fig. 9). Among models, VR-CESM 0.125° and WRF-9 matched most closely to SNOTEL, but both had an early SCD bias. The SCD in VR-CESM 0.125° falls around water yearday 170 (21 March), the closest match to SNOTEL across all model datasets. SCD for WRF-9 falls around water yearday 160 (11 March), around 2 weeks before the expected date. Melt rate and the date on which the complete melt of SWE occurs differentiated VR-CESM 0.125° and WRF-9, with WRF-9 more closely matching SNOTEL. The melt rate in VR-CESM 0.125° was too rapid, resulting in a complete melt occurring approximately 30 days sooner than in the SNOTEL dataset. Daymet had a late SCD around day 191 (10 April), 10 days after SNOTEL. The melt rate in the Daymet dataset was much slower than in all other datasets. Further, since Daymet analyzed each year in isolation, the snowpack was discontinuous at water yearday 91 (Thornton et al. 2014). Snowpack accumulation onset matched fairly well across all datasets, with the onset date around water yearday 36 (5 November). Within the 28-km simulations, most model datasets seem to match in terms of having an earlier expected SCD clustered on water yearday 151 (1 March), approximately 30 days sooner than SNOTEL. The remapped version of Daymet at 0.25° showed a similar late SCD bias (water yearday 191) and

showed a more drastic slowdown in melt rate. All 0.25° datasets matched fairly well in snowmelt rate and accumulation onset, matching well with SNOTEL. Full melt generally occurred earlier (water yearday 240) across models relative to SNOTEL (water yearday 270). In the 1° datasets, CESM-SE 1° had a physically unreasonable SCD (water yearday 90), snowmelt rate, and accumulation onset date. Of interest is that, at the 1° resolution, the biases in Daymet are minimized and the SCD, snowmelt rate, date of complete melt, and accumulation onset date all are well within the range of SNOTEL.

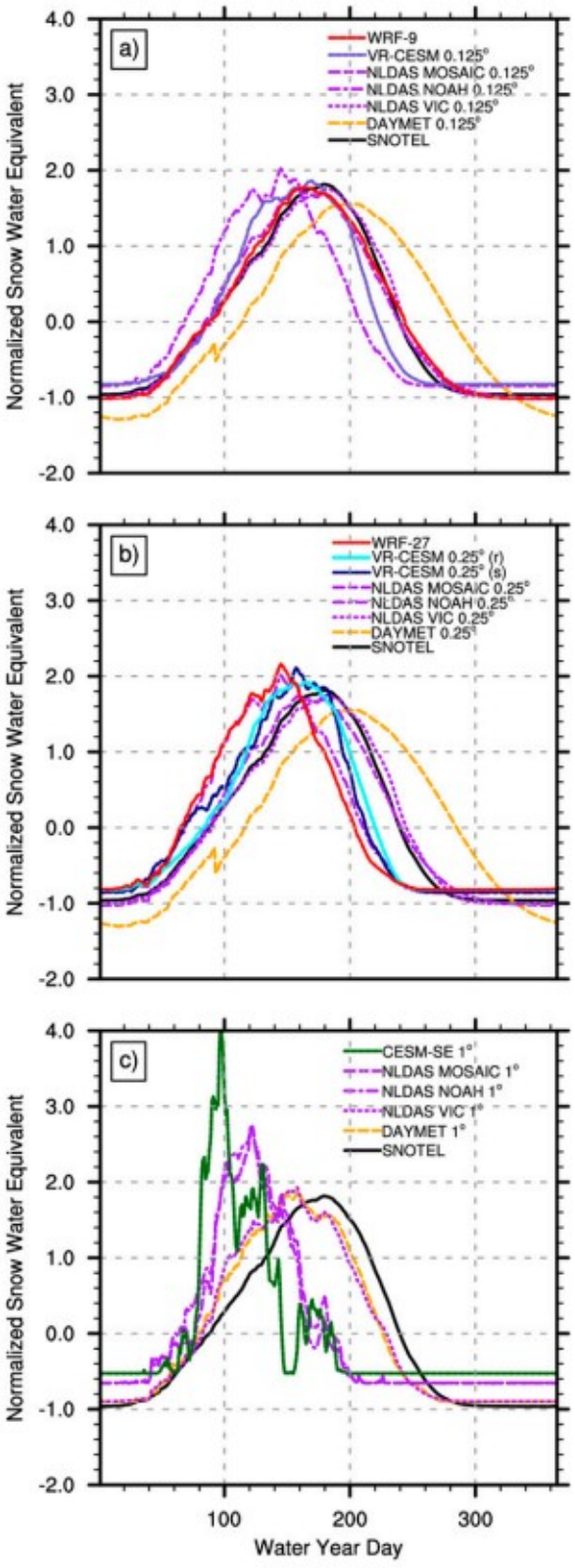


FIG. 9. As in Fig. 8, but for normalized average SWE. The Sierra Nevada SNOTEL station dataset (19 locations) is plotted in black within each diagram.

f. Linear trends in DJF seasonal snowpack

Figure 10 highlights the linear trend in DJF seasonal mean SWE values for the historical period in the Sierra Nevada SNOTEL subregion. For comparison, the 19 SNOTEL station datasets are plotted in the upper-left panel. The gray lines indicate individual SNOTEL stations, with the mean SNOTEL-station seasonal trend shown in black and the linear trend line in red. Each of the model and reanalysis datasets is plotted using similar axis bounds, except for WRF-9, which exhibited larger values of SWE. SNOTEL stations are plotted with a larger axis, representative of these observations being pointwise measurements in regions of greater snow accumulation. The general trend across VR-CESM simulations is a slight decrease in DJF seasonal mean SWE. VR-CESM 0.125° had the largest negative trend at $-0.198$ mm $yr^{-1}$, with VR-CESM 0.25° (smooth) at $-0.093$ mm $yr^{-1}$ and VR-CESM 0.25° (rough) at $-0.029$ mm $yr^{-1}$. Except when compared with Cal-Adapt, which shows a dramatic increase in SWE, and Daymet, which shows a faster decrease in SWE, the general trends for VR-CESM datasets are slightly more negative than for the SNOTEL and NLDAS reanalysis datasets. This result is corroborated by Mote et al. (2005) who found a 2.2% decline in mean 1 April SWE across the in situ snowpack observational stations within the Sierra Nevada over the historical record [i.e., 1990–97 (final period) minus 1945–50 (initial period)], with inclusion of snow-course data also. Of interest is that the 19 sampled SNOTEL stations showed a nearly flat trend (0.016 mm $yr^{-1}$) in DJF mean seasonal SWE over the study period. WRF simulations showed differing results, with WRF-9 showing an exceedingly strong positive trend (0.410 mm $yr^{-1}$) in mean seasonal SWE and WRF-27 having a stagnant to slightly positive trend (0.011 mm $yr^{-1}$), matching most closely with SNOTEL. CESM-SE 1° and CESM-FV 0.25° both had a negative trend in mean seasonal SWE, with magnitudes of $-0.259$ and $-0.200$ mm $yr^{-1}$, respectively.

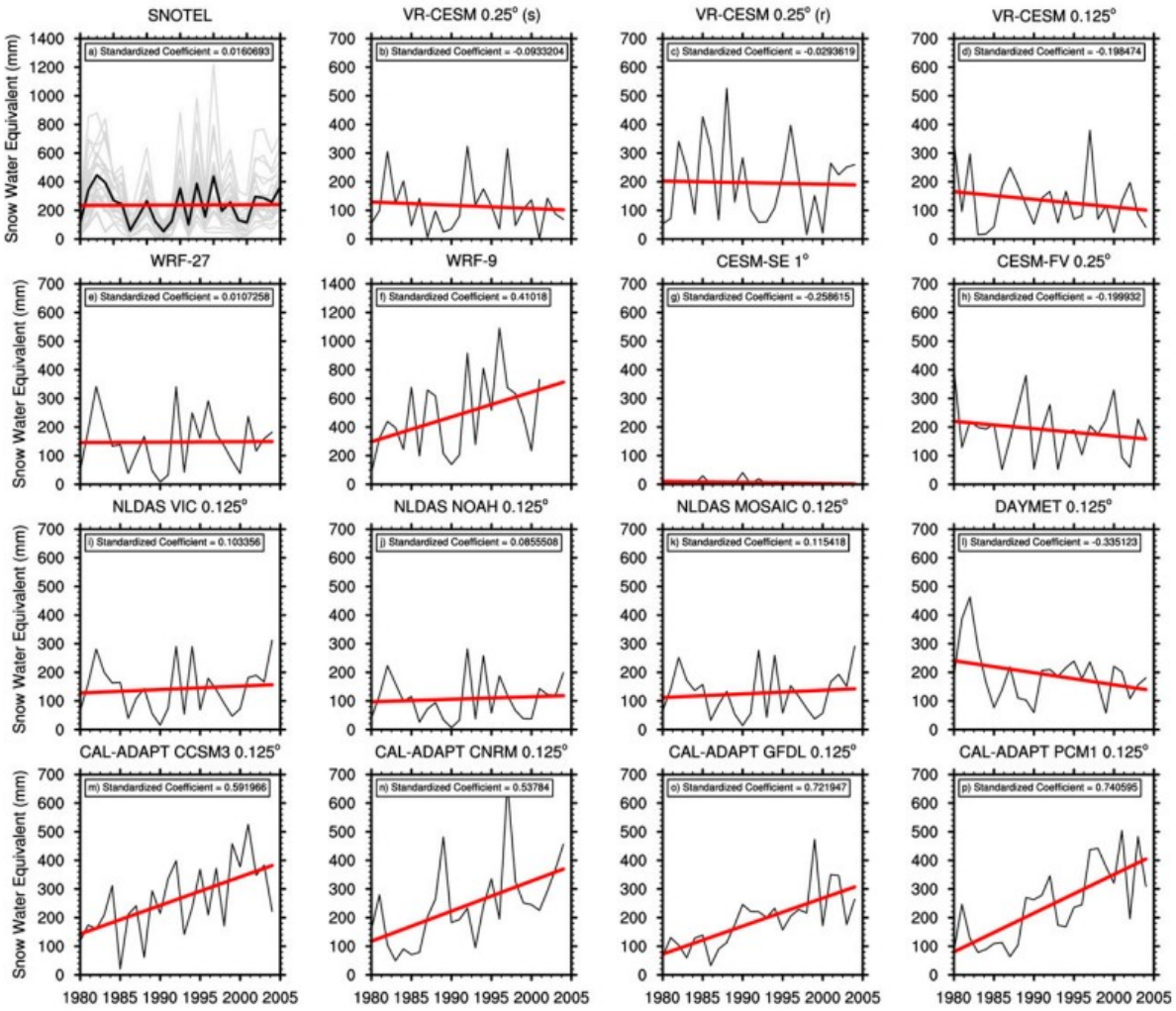


FIG. 10. Linear trend (red lines) in average seasonal DJF SWE within the Sierra Nevada SNOTEL comparison subregion across model, observational, and reanalysis datasets over the historical period (DJF seasons for 1980–2005; black lines). The standardized regression coefficient is shown at the top of each panel. [(a) The SNOTEL dataset, incorporating 19 SNOTEL stations spread throughout the Sierra Nevada that contained 25 DJF seasons of observations. Gray lines indicate individual SNOTEL stations, with the average seasonal DJF SWE value represented by the black line.]

## g. SNOWC summary statistics

Figure 11 represents average climatological DJF SNOWC plotted for all datasets over California. Similar to SWE, an increase in resolution results in a much more heterogeneous representation of SNOWC properties that is more closely matched to observations, as represented by 12 seasons of MODIS (MODIS-5) data. A topographic influence is clearly seen as resolution is increased, with higher-resolution models capturing lower-elevation basins that are otherwise smoothed out. This resolution dependence manifests itself in statistical calculations of average DJF SNOWC within the Sierra Nevada (Table 4). WRF-9 showed the closest match to mean seasonal SNOWC, with a value only 1.5% lower than that for the MODIS dataset. VR-CESM 0.25° (rough) and VR-CESM 0.125° were the next closest with a slightly more conservative estimate (7% below MODIS) of SNOWC. All other datasets,

except CESM-FV 0.25°, which had a positive bias of ~8%, had much smaller estimates of mean seasonal SNOWC. CESM-SE 1° provided the largest underestimate among the model datasets with mean seasonal values at one-quarter of the comparable remapped version of MODIS. Interestingly, two of the best available high-resolution reanalysis datasets (NCEP and NARR) seem unable to capture properly the Sierra Nevada SNOWC characteristics in the MODIS dataset, with most of the reanalysis datasets showing a negative bias for SNOWC. NARR-32 and NCEP-35 had mean SNOWC values from one-half to two-thirds of the value indicated by MODIS, and NLDAS VIC, Noah, and Mosaic were at 84%, 74%, and 47% of MODIS, respectively. The median values for DJF SNOWC for VR-CESM 0.125° and VR-CESM 0.25° showed a close approximation to those seen in NLDAS VIC. As expected, since SNOWC is capped at 100%, maximum DJF SNOWC was reached by most modeling platforms.

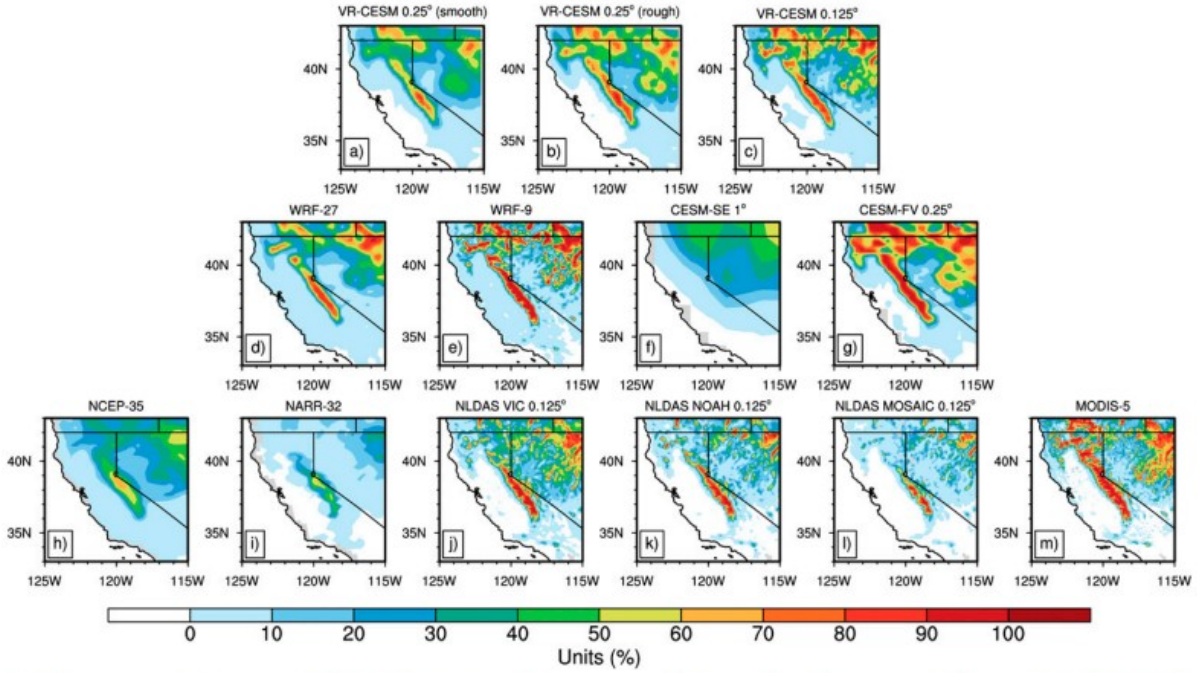


FIG. 11. Average climatological DJF SNOWC across model, observational, and reanalysis datasets over California. [(m) The MODIS dataset spans 2000–12.]

TABLE 4. As in Table 2, but for SNOWC.

| Model | DJF seasons | Mean | Std dev | Lower quartile | Median | Upper quartile | Max | Sierra Nevada mask points |
|---|---|---|---|---|---|---|---|---|
| VR-CESM 0.25° (smooth) | 25 | 40.0 | 30.1 | 13.6 | 36.5 | 62.5 | 100 | 2175 |
| VR-CESM 0.25° (rough) | 25 | 48.9 | 33.5 | 17.5 | 46.7 | 81.6 | 100 | 2175 |
| VR-CESM 0.125° | 25 | 48.7 | 30.3 | 22.0 | 47.8 | 74.1 | 100 | 2175 |
| WRF-27 | 25 | 42.9 | 30.1 | 15.3 | 40.0 | 67.2 | 98.0 | 2175 |
| WRF-9 | 22 | 55.0 | 37.3 | 16.3 | 58.6 | 96.7 | 98.0 | 14 058 |
| WRF-9 (regrid 0.125°) | 22 | 54.3 | 35.6 | 19.1 | 56.3 | 92.3 | 98.0 | 7721 |
| CESM-SE 1° | 25 | 9.10 | 12.3 | 0.60 | 4.40 | 11.9 | 60.3 | 150 |
| CESM-FV 0.25° | 25 | 62.8 | 32.2 | 36.6 | 69.9 | 92.3 | 100.0 | 2175 |
| NCEP-35 | 25 | 37.1 | 25.5 | 15.3 | 33.7 | 56.5 | 96.6 | 1350 |
| NARR-32 | 25 | 22.5 | 27.5 | 0.60 | 9.60 | 37.5 | 100 | 1175 |
| MODIS-5 | 12 | 56.7 | 36.6 | 18.0 | 65.0 | 93.0 | 100 | 25 932 |
| MODIS-5 (regrid 0.125°) | 12 | 55.8 | 35.8 | 18.5 | 62.8 | 90.7 | 100 | 4188 |
| MODIS-5 (regrid 0.25°) | 12 | 55.0 | 36.0 | 16.3 | 61.4 | 90.8 | 100 | 1032 |
| MODIS-5 (regrid 1°) | 12 | 37.6 | 33.1 | 3.80 | 34.0 | 69.1 | 95.7 | 60 |
| NLDAS VIC 0.125° | 25 | 46.6 | 33.0 | 15.0 | 45.9 | 75.9 | 100 | 8742 |
| NLDAS VIC 0.25° | 25 | 46.8 | 33.3 | 14.9 | 45.1 | 78.4 | 100 | 2166 |
| NLDAS VIC 1.00° | 25 | 32 | 25.4 | 11.6 | 26.6 | 45.8 | 87.5 | 149 |
| NLDAS Noah 0.125° | 25 | 41.5 | 33.8 | 7.60 | 37.5 | 71.6 | 100 | 8720 |
| NLDAS Noah 0.25° | 25 | 42.1 | 34.3 | 8.30 | 38.4 | 73.4 | 100 | 2164 |
| NLDAS Noah 1.00° | 25 | 25.9 | 25.4 | 4.10 | 18.3 | 40.7 | 85.0 | 149 |
| NLDAS Mosaic 0.125° | 25 | 26.4 | 29.6 | 1.40 | 13.1 | 45.4 | 98.8 | 8722 |
| NLDAS Mosaic 0.25° | 25 | 26.8 | 30.1 | 1.40 | 13.1 | 47.6 | 98.2 | 2163 |
| NLDAS Mosaic 1.00° | 25 | 12.8 | 18.8 | 0.30 | 4.20 | 14.4 | 66.7 | 149 |
| Reanalysis-dataset avg 0.125° | — | 42.6 | 33.1 | 10.6 | 39.8 | 70.9 | 99.7 | — |
| Reanalysis-dataset avg 0.25° | — | 42.7 | 33.5 | 10.2 | 39.5 | 72.6 | 99.6 | — |

## h. Seasonal variability in snow cover

Mean seasonal variability (interannual standard deviation of the seasonal mean) in SNOWC is shown over California (Fig. 12). Standard-deviation values for each of the simulations are given in Table 4. As with the mean seasonal SNOWC values, WRF-9 had the best representation of seasonal variability within the Sierra Nevada, with a close approximation to standard-deviation values in the remapped MODIS dataset (although it underestimates standard deviation in the lee of the Sierra Nevada). VR-CESM 0.25° (rough) also was able to characterize seasonal variability at a realistic level, with a standard deviation only 14% below that of MODIS. All other modeling platforms had a conservative estimate of variability, ranging from one-half to three-quarters of the observed standard deviation, when compared with common remapped resolutions. This result is apparent in Fig. 13 for each dataset and in analyzing the IQRs. All datasets, save for WRF-9 and CESM-FV 0.25°, had a conservative estimate of SNOWC summary statistics when compared with MODIS. Median values, along with IQRs, are too low, with a noticeable bias in the 75th percentiles.

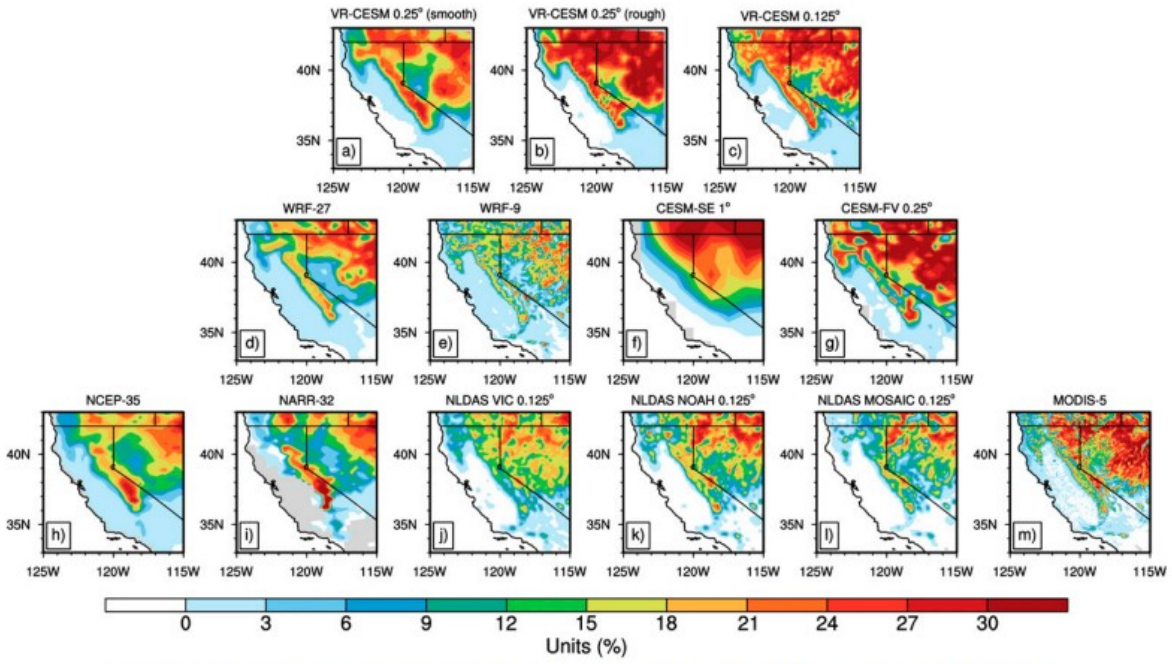


FIG. 12. As in Fig. 11, but for average DJF variability (interannual std dev of the seasonal mean) of SNOWC.

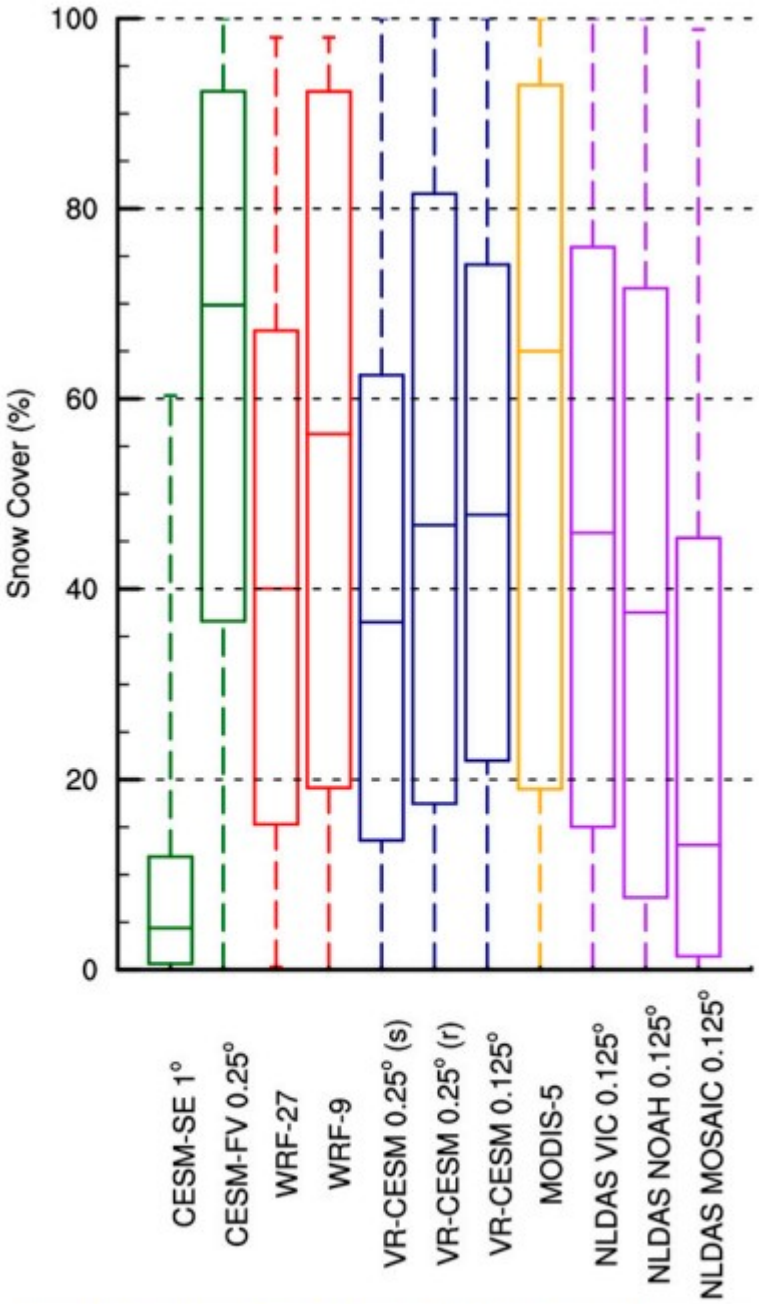


FIG. 13. Similar to Fig. 6, but for SNOWC. Regridding of reanalysis datasets to 0.25° (or 0.125° for MODIS) had no noticeable effect on the statistics and so is not shown. The MODIS dataset spans 2000–12.

i. Pattern correlation and bias in snow cover

The average seasonal centered Pearson product-moment coefficients and mean climatological bias for SNOWC are exhibited in Table 5. MODIS was not used in the centered Pearson calculations because it only spanned five years of the historical period (2000–05). A close match was seen across both VR-

CESM and WRF modeling platforms when compared with the three NLDAS datasets. Most values fell around 0.74 for the VR-CESM simulations and 0.84 for the WRF simulations. The CESM-FV and CESM-SE had the lowest correlations at 0.53 and 0.15, respectively. The smallest mean climatological bias in DJF SNOWC between MODIS and the model datasets was for VR-CESM 0.125°, VR-CESM 0.25° (rough), and WRF-27, with negative biases of approximately 6%–7%. CESM-SE 1° produced the worst match across model datasets, with a −28.5% bias. Of note is that the NLDAS reanalysis datasets also widely varied in their ability to characterize mean climatological SNOWC bias when compared with MODIS, with consistent negative biases ranging between −9.2% (NLDAS VIC) and −29.4% (NLDAS Mosaic).

TABLE 5. As in Table 3, but for SNOWC.

| Model | VR-CESM 0.125° | VR-CESM 0.25° (rough) | VR-CESM 0.25° (smooth) | WRF-9 | WRF-27 | CESM-FV 0.25° | CESM-SE 1° |
|---|---|---|---|---|---|---|---|
| | | | DJF climate bias (mm) | | | | |
| NLDAS VIC | 2.10 | 2.10 | −6.80 | −3.70 | 1.90 | 16.0 | −22.9 |
| NLDAS Noah | 7.20 | 6.80 | −2.10 | 1.40 | 6.60 | 20.7 | −16.8 |
| NLDAS Mosaic | 22.3 | 22.1 | 13.2 | 16.5 | 21.9 | 36.0 | −3.70 |
| MODIS-5 | −7.10 | −6.10 | −15.0 | −12.9 | −6.30 | 7.80 | −28.5 |
| Reanalysis-dataset absolute-value avg | 9.70 | 9.30 | 9.30 | 8.60 | 9.20 | 20.1 | 18.0 |
| | | | DJF Pearson pattern correlation | | | | |
| NLDAS VIC | 0.76 | 0.79 | 0.77 | 0.92 | 0.84 | 0.56 | 0.24 |
| NLDAS Noah | 0.78 | 0.80 | 0.77 | 0.92 | 0.85 | 0.60 | 0.17 |
| NLDAS Mosaic | 0.65 | 0.69 | 0.68 | 0.78 | 0.76 | 0.44 | 0.04 |
| Reanalysis-dataset avg | 0.73 | 0.76 | 0.74 | 0.87 | 0.82 | 0.53 | 0.15 |

## 5. Discussion and conclusions

The primary goal of this paper has been to assess the efficacy of VR-CESM in simulating the mean climatological state and seasonal variability within Sierra Nevada snowpack metrics (i.e., SWE, SCD, and SNOWC). It was determined that the efficacy of the VR-CESM framework in simulating climatological mean and seasonal variability in both SWE and SNOWC was competitive with traditional dynamical downscaling. Overall, given California's complex terrain and intermittent climate, a 0.68 centered correlation (less correlated yet similar to values seen in WRF), a negative mean SWE bias of <7 mm, and an IQR well within the range of values exhibited in the best available spatially continuous datasets for SWE together confirm the ability of both VR-CESM 0.25° (rough) and VR-CESM 0.125° to simulate SWE on both climatological and seasonal scales. Of note is that both of the VR-CESM simulations were solely constrained by prescribed SST and sea ice data, whereas WRF simulations were further constrained at lateral boundaries by ERA-Interim data (in addition to SST and sea ice), yet both showed comparable statistical properties. This was similarly confirmed for the climatological mean for DJF SNOWC, for which both the VR-CESM 0.125° and VR-CESM 0.25° (rough) simulations were within 7% of the expected mean MODIS value. VR-CESM 0.25° (rough) was

able to characterize MODIS's standard deviation well (86% match). WRF-9 had the best representation of SNOWC, with a near identical representation in mean, standard deviation, and IQR when compared with MODIS, but at the cost of unreasonably high SWE values. This is likely indicative of the overexaggeration of topography at higher resolutions in the model, where the fractal nature of peaks and, more important, valleys are misrepresented (cf. ETOPO2v2 with model topography in Fig. 2), leading to a bias in overall snowpack characterizations. VR-CESM, as well as WRF, conveyed mixed results in representing seasonal variability in SWE (average standard-deviation value at each grid point), with generally conservative estimates across all assessed modeling platforms except WRF-9 and CESM-FV 0.25°, which had much higher estimates. The total water content of snowpack within the Sierra Nevada was best represented in both VR-CESM 0.125° and VR-CESM 0.25° (rough) when compared with the remapped NLDAS VIC reference dataset at their respective resolutions. VR-CESM 0.125° and WRF-9 showcased the best representation, across datasets, of SCD timing, snowmelt rate, and snowpack accumulation onset in comparison with SNOTEL. The two datasets differed in the date on which complete melting of SWE occurred, with VR-CESM 0.125° occurring too early whereas WRF-9 had a slightly late onset. It is interesting that both SWE and SNOWC did not show a significant enhancement in snowpack properties when VR-CESM resolution was moved from 0.25° to 0.125°; in fact, the 0.25° simulation [VR-CESM 0.25° (rough)] was slightly more skillful when considering all metrics. Topographical roughness was found to play a much more significant role in representing snowpack properties, with VR-CESM 0.25° (rough) seeing a 16-fold decrease in average seasonal SWE bias, a threefold increase in SWE seasonal variability, an IQR increase from 48.9 to 64.1, and a considerable increase in the SCD total water content for the Sierra Nevada. These results are an improvement when compared with the average of all of the reanalysis datasets. Furthermore, DJF temperature characteristics may have played a role in modulating which of the simulations performed most optimally. Figure 14 highlights average climatological DJF 2-m surface temperatures for only the model simulations. Below-freezing (<273 K) temperatures are shown to be maintained over greater areas for the climatic period across all higher-resolution (≤0.25°) simulations, likely because of increased topographic elevations in those areas. This temperature maintenance likely drives winter-season snowpack accumulation and sustainment.

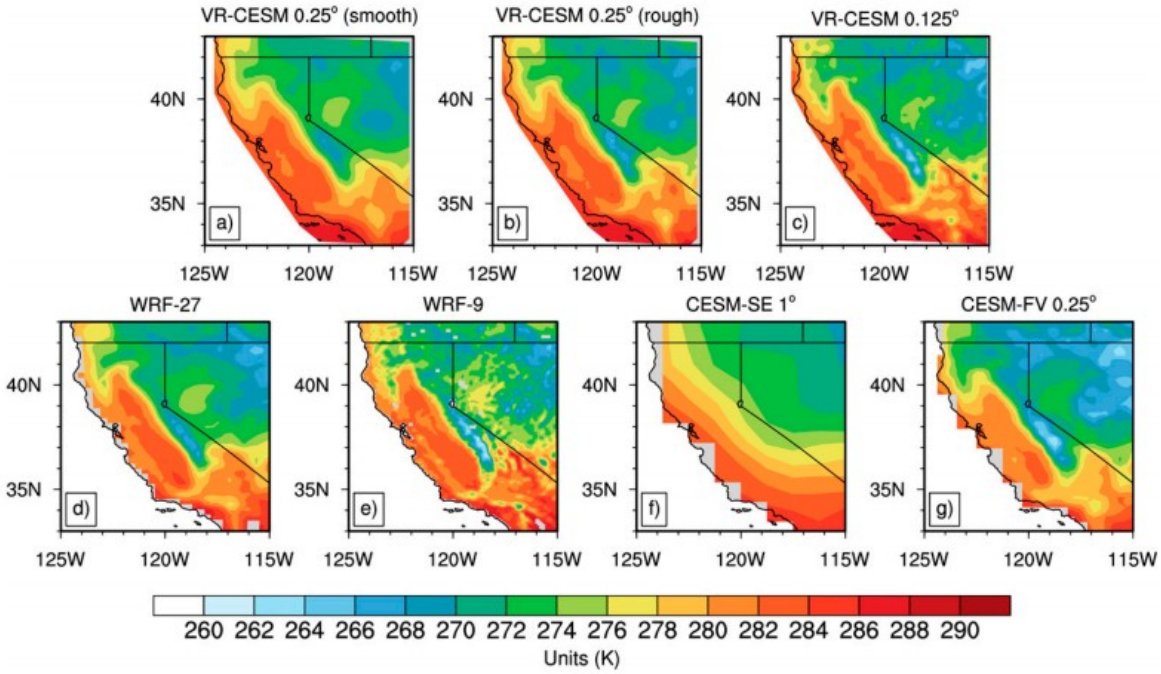


FIG. 14. Average climatological DJF 2-m surface temperature across model datasets over California.

The VR-CESM framework provides greatly enhanced representation of snowpack properties relative to widely used GCMs (i.e., CESM-FV 1° and CESM-FV 0.25°). Simulation of Sierra Nevada snowpack in the VR-CESM framework is competitive with traditional dynamical downscaling techniques but has the additional means of providing dynamic interaction with large-scale atmosphere–ocean drivers and teleconnections that might not otherwise manifest in an RCM constrained by boundary conditions. These two points lend them themselves well to using certain versions of VR-CESMs [viz., VR-CESM 0.25° (rough) and VR-CESM 0.125°] in projecting future climate-change scenarios and their resultant impacts on water resources over the western United States.

The topographical smoothing between the two VR-CESM 0.25° simulations had the most dramatic influence on snowpack-product tendencies found within the VR-CESM framework, even when compared with changes resulting from a doubling of model resolution from 0.25° to 0.125°. As shown in Table 2, mean seasonal SWE for the Sierra Nevada nearly doubled from 50.4 to 95.2 mm between VR-CESM 0.25° (smooth) and VR-CESM 0.25° (rough), with a decrease in average DJF climate bias in SWE from −52% to −2.3% when compared with the reanalysis-dataset average. This tendency was similar for the lower-quartile, median, and higher-quartile values. In a similar way, the seasonal variability, indicated by the standard-deviation plots (Fig. 5) and standard-deviation values (Table 2), nearly tripled, making the VR-CESM 0.25° (rough) simulation the closest match to the reanalysis-dataset average within all model simulations. Changes in SNOWC trends were also apparent,

although they were less dramatic than those for SWE (Table 4). Average seasonal SNOWC increased by 9%, and the IQR increased from 48.9 to 64.1, matching more closely to the MODIS dataset value of 74.5, with the higher quartile being less conservatively biased.

Improved topographical resolution also resulted in better representation of the snow characteristics of the maritime mountain ranges (e.g., the Cascades and the Coast Ranges) (Fig. 4). Maritime mountain ranges have shown some of the greatest snowpack decreases over the historical record (Serreze et al. 1999; Mote 2003; Mote et al. 2005) and are in need of the best available climate-change impact analysis because of a greater susceptibility to climate-change trends (i.e., warmer and potentially more precipitous weather fronts originating from relatively warmer ocean waters). This is important because conventional GCM simulations are generally performed at resolutions that are too coarse to properly resolve the aforementioned topographical forcings and thus may bias evaluations used to guide climate-impact studies and climate-policy formulation. This is not to say that the VR-CESM framework provides perfect representation of these ranges but that it provides a more realistic and computationally effective means to characterize these ranges in a changing climate. This subject will be the target of further research.

A higher-resolution surface dataset for PFTs would have been beneficial for this study so as to capitalize on the higher-resolution (<0.5°) VR-CESM grids that were implemented into CLM, but none were available at the time of writing. An extensive review of the North American and European literature on snowpack–canopy interaction by Varhola et al. (2010) argued that snowpack accumulation and melting patterns can be significantly altered by changes in forest cover, accounting for relative variance changes of 57% in snow accumulation and 72% in snow ablation. After discussion with the CLM development team at NCAR, a 2-min PFT dataset for the year 2000 was identified. This dataset will be used in future simulations to assess the effects of canopy interactions on snowpack metrics within a VR-CESM framework.

Added benefits of the VR-CESM framework, not discussed previously, include the large enhancement in computational efficiency. For example, the 0.25° (0.125°) VR-CESM grid had approximately 8400 (11 300) elements. When compared with conventional uniform resolution grids at 1.00°, 0.25°, or 0.125°, which have 5400, 86 400, and 345 600 elements, respectively, a theoretical speedup in computation time of 10–30 times is expected for the VR-CESM framework, with the assumption of linear computational scalability highlighted in Dennis et al. (2011) and Zarzycki et al. (2014a). Therefore, for a relatively similar computational cost of a uniform 1.00° grid, one can get vastly improved snowpack-product characteristics over a limited region of interest, especially within the California Sierra Nevada. This is not only a function of resolving smaller-scale meteorological features but is also due to better representations of topography and, in some cases, land-surface

properties. Therefore, for only a fraction of the cost of a high-resolution uniform GCM run, the VR-CESM approach can be performed on a local server (<1000 processors), with 20–40-day turnarounds on 25-yr simulation periods and can provide model resolutions from 0.25° (28 km) to 0.125° (14 km), which decision makers (especially in the western U.S. water sector), may find more useful in regional-planning endeavors. The enhanced representation of snowpack and the relative computational efficiency of VR-CESM lend themselves well to future investigations of other SWE-dependent regions of the western United States, as well as to ensemble-based climate-change-scenario analysis.

## Acknowledgments

The authors acknowledge the computational support and patience provided by the University of California, Davis, Farm Cluster IT support team (i.e., Bill Broadley and Terri Knight). We also thank all reviewers for their helpful comments. We believe the quality of the manuscript is greatly improved after incorporating their suggestions. Further, the fruitful conversations with Alison Whipple, Dustin Grogan, and Nicolas Bambach throughout the production of this paper were indispensable and truly appreciated. This research was funded by the National Science Foundation (NSF) via the Climate Change, Water, and Society Integrated Graduate Education and Research Traineeship (IGERT) program at the University of California, Davis (NSF Award Number 1069333), the Leland Roy Saxon and Georgia Wood Saxon Fellowship, and the U.S. Department of Energy Office of Science project “Multiscale Methods for Accurate, Efficient, and Scale-Aware Models of the Earth System.”

## References

Anderson, E. A., 1976: A point of energy and mass balance model of snow cover. NOAA Tech. Rep. NWS 19, 172 pp. [Available online at http://amazon.nws.noaa.gov/articles/HRL_Pubs_PDF_May12_2009/HRL_PUBS_51-100/81_A_POINT_ENERGY_AND_MASS.pdf.]

Bales, R. C., N. P. Molotch, T. H. Painter, M. D. Dettinger, R. Rice, and J. Dozier, 2006: Mountain hydrology of the western United States. *Water Resour. Res.*, 42, W08432, doi:https://doi.org/10.1029/2005WR004387.

Bales, R. C., J. J. Battles, Y. Chen, M. H. Conklin, E. Holst, K. L. O’Hara, P. Saksa, and W. Stewart, 2011: Forests and water in the Sierra Nevada: Sierra Nevada watershed ecosystem enhancement project. Sierra Nevada Research Institute Rep. 11.1, 39 pp. [Available online at http://ucanr.edu/sites/cff/files/146199.pdf.]

Caldwell, P., 2010: California wintertime precipitation bias in regional and global climate models. *J. Appl. Meteor. Climatol.*, 49, 2147–2158, doi:https://doi.org/10.1175/2010JAMC2388.1.

Cayan, D. R., 1996: Interannual climate variability and snowpack in the western United States. *J. Climate*, 9, 928–948, doi:https://doi.org/10.1175/1520-0442(1996)009<0928:ICVASI>2.0.CO;2.

Cayan, D. R., K. T. Redmond, and L. G. Riddle, 1999: ENSO and hydrologic extremes in the western United States. *J. Climate*, 12, 2881–2893, doi:https://doi.org/10.1175/1520-0442(1999)012<2881:EAHEIT>2.0.CO;2.

Chen, F., and J. Dudhia, 2001: Coupling an advanced land surface–hydrology model with the Penn State–NCAR MM5 modeling system. Part I: Model implementation and sensitivity. *Mon. Wea. Rev.*, 129, 569–585, doi:https://doi.org/10.1175/1520-0493(2001)129<0569:CAALSH>2.0.CO;2.

Collins, W. D., and Coauthors, 2004: Description of the NCAR Community Atmosphere Model (CAM 3.0). National Center for Atmospheric Research Tech. Rep. NCAR/TN-464+STR, 214 pp. [Available online at http://www.cesm.ucar.edu/models/atm-cam/docs/description/description.pdf. ]

Dee, D., and Coauthors, 2011: The ERA-Interim reanalysis: Configuration and performance of the data assimilation system. *Quart. J. Roy. Meteor. Soc.*, 137, 553–597, doi:https://doi.org/10.1002/qj.828.

DeFlorio, M. J., D. W. Pierce, D. R. Cayan, and A. J. Miller, 2013: Western U.S. extreme precipitation events and their relation to ENSO and PDO in CCSM4. *J. Climate*, 26, 4231–4243, doi:https://doi.org/10.1175/JCLI-D-12-00257.1.

Dennis, J., and Coauthors, 2011: CAM-SE: A scalable spectral element dynamical core for the Community Atmosphere Model. *Int. J. High Perform. Comput. Appl.*, 26, 74–89, doi:https://doi.org/10.1177/1094342011428142.

Dettinger, M. D., 2011: Climate change, atmospheric rivers, and floods in California—A multimodel analysis of storm frequency and magnitude changes. *J. Amer. Water Resour. Assoc.*, 47, 514–523, doi:https://doi.org/10.1111/j.1752-1688.2011.00546.x.

Dettinger, M. D., D. R. Cayan, H. F. Diaz, and D. M. Meko, 1998: North-south precipitation patterns in western North America on interannual-to-decadal timescales. *J. Climate*, 11, 3095–3111, doi:https://doi.org/10.1175/1520-0442(1998)011<3095:NSPPIW>2.0.CO;2.

Dettinger, M. D., F. M. Ralph, T. Das, P. J. Neiman, and D. R. Cayan, 2011: Atmospheric rivers, floods and the water resources of California. *Water*, 3, 445–478, doi:https://doi.org/10.3390/w3020445.

Fang, C., L. Wu, and X. Zhang, 2014: The impact of global warming on the Pacific decadal oscillation and the possible mechanism. *Adv. Atmos. Sci.*, 31, 118–130, doi:https://doi.org/10.1007/s00376-013-2260-7.

Gates, W. L., 1992: AMIP: The atmospheric model intercomparison project. *Bull. Amer. Meteor. Soc.*, 73, 1962–1970, doi:https://doi.org/10.1175/1520-0477(1992)073<1962:ATAMIP>2.0.CO;2.

Ghan, S. J., X. Liu, R. C. Easter, R. Zaveri, P. J. Rasch, J.-H. Yoon, and B. Eaton, 2012: Toward a minimal representation of aerosols in climate models: Comparative decomposition of aerosol direct, semidirect, and indirect radiative forcing. *J. Climate*, 25, 6461–6476, doi:https://doi.org/10.1175/JCLI-D-11-00650.1.

Gimeno, L., R. Nieto, M. Vázquez, and D. A. Lavers, 2014: Atmospheric rivers: A mini-review. *Front. Earth Sci.*, 2, doi:https://doi.org/10.3389/feart.2014.00002.

Glantz, M. H., R. W. Katz, and N. Nicholls, Eds., 1991: *Teleconnections Linking Worldwide Climate Anomalies.* Cambridge University Press, 535 pp.

Guan, B., N. P. Molotch, D. E. Waliser, E. J. Fetzer, and P. J. Neiman, 2010: Extreme snowfall events linked to atmospheric rivers and surface air temperature via satellite measurements. *Geophys. Res. Lett.*, 37, L20401, doi:https://doi.org/10.1029/2010GL044696.

Guan, B., N. P. Molotch, D. E. Waliser, E. J. Fetzer, and P. J. Neiman, 2013: The 2010/2011 snow season in California's Sierra Nevada: Role of atmospheric rivers and modes of large-scale variability. *Water Resour. Res.*, 49, 6731–6743, doi:https://doi.org/10.1002/wrcr.20537.

Hall, D. K., and G. A. Riggs, 2007: Accuracy assessment of the MODIS snow products. *Hydrol. Processes*, 21, 1534–1547, doi:https://doi.org/10.1002/hyp.6715.

Hall, D. K., G. A. Riggs, and V. V. Salomonson, 2006: Modis snow and sea ice products. *Earth Science Satellite Remote Sensing*, J. J. Qu et al., Eds., Springer, 154–181.

Hanak, E., and J. R. Lund, 2012: Adapting California's water management to climate change. *Climatic Change*, 111, 17–44, doi:https://doi.org/10.1007/s10584-011-0241-3.

Hong, S.-Y., and J.-O. J. Lim, 2006: The WRF single-moment 6-class microphysics scheme (WSM6). *J. Korean Meteor. Soc.*, 42 (2), 129–151. [Available online at http://www2.mmm.ucar.edu/wrf/users/docs/WSM6-hong_and_lim_JKMS.pdf.]

Hong, S.-Y., Y. Noh, and J. Dudhia, 2006: A new vertical diffusion package with an explicit treatment of entrainment processes. *Mon. Wea. Rev.*, 134, 2318–2341, doi:https://doi.org/10.1175/MWR3199.1.

Iacono, M. J., J. S. Delamere, E. J. Mlawer, M. W. Shephard, S. A. Clough, and W. D. Collins, 2008: Radiative forcing by long-lived greenhouse gases: Calculations with the AER radiative transfer models. *J. Geophys. Res.*, 113, D13103, doi:https://doi.org/10.1029/2008JD009944.

Jordan, R., 1991: A one-dimensional temperature model for a snow cover: Technical documentation for SNTHERM. 89. Cold Regions Research and

Engineering Laboratory Special Rep. 91-16, 62 pp. [Available online at http://acwc.sdp.sirsi.net/client/en_US/search/asset/1011960.]

Kain, J. S., 2004: The Kain–Fritsch convective parameterization: An update. *J. Appl. Meteor.*, 43, 170–181, doi:https://doi.org/10.1175/1520-0450(2004)043<0170:TKCPAU>2.0.CO;2.

Kapnick, S., and A. Hall, 2012: Causes of recent changes in western North American snowpack. *Climate Dyn.*, 38, 1885–1899, doi:https://doi.org/10.1007/s00382-011-1089-y.

Lawrence, D. M., and Coauthors, 2011: Parameterization improvements and functional and structural advances in version 4 of the Community Land Model. *J. Adv. Model. Earth Syst.*, 3, doi:https://doi.org/10.1029/2011MS000045.

Li, W., and C. E. Forest, 2014: Estimating the sensitivity of the atmospheric teleconnection patterns to SST anomalies using a linear statistical method. *J. Climate*, 27, 9065–9081, doi:https://doi.org/10.1175/JCLI-D-14-00231.1.

Maurer, E. P., and H. G. Hidalgo, 2008: Utility of daily vs. monthly large-scale climate data: An intercomparison of two statistical downscaling methods. *Hydrol. Earth Syst. Sci.*, 12, 551–563, doi:https://doi.org/10.5194/hess-12-551-2008.

Mesinger, F., and Coauthors, 2006: North American Regional Reanalysis. *Bull. Amer. Meteor. Soc.*, 87, 343–360, doi:https://doi.org/10.1175/BAMS-87-3-343.

Montoya, E., J. Dozier, and W. Meiring, 2014: Biases of April 1 snow water equivalent records in the Sierra Nevada and their associations with large-scale climate indices. *Geophys. Res. Lett.*, 41, 5912–5918, doi:https://doi.org/10.1002/2014GL060588.

Morrison, H., and A. Gettelman, 2008: A new two-moment bulk stratiform cloud microphysics scheme in the Community Atmosphere Model, version 3 (CAM3). Part I: Description and numerical tests. *J. Climate*, 21, 3642–3659, doi:https://doi.org/10.1175/2008JCLI2105.1.

Mote, P. W., 2003: Trends in snow water equivalent in the Pacific Northwest and their climatic causes. *Geophys. Res. Lett.*, 30, 1601, doi:https://doi.org/10.1029/2003GL017258.

Mote, P. W., A. F. Hamlet, M. P. Clark, and D. P. Lettenmaier, 2005: Declining mountain snowpack in Western North America. *Bull. Amer. Meteor. Soc.*, 86, 39–49, doi:https://doi.org/10.1175/BAMS-86-1-39.

Neale, R. B., J. H. Richter, and M. Jochum, 2008: The impact of convection on ENSO: From a delayed oscillator to a series of events. *J. Climate*, 21, 5904–5924, doi:https://doi.org/10.1175/2008JCLI2244.1.

Neale, R. B., and Coauthors, 2010: Description of the NCAR Community Atmosphere Model (CAM 5.0). National Center for Atmospheric Research

Tech. Note NCAR/TN-486+STR, 268 pp. [Available online at http://www.cesm.ucar.edu/models/cesm1.0/cam/docs/description/cam5_desc.pdf.]

NGDC, 2006: 2-minute Gridded Global Relief Data (ETOPO2) v2. NOAA/National Geophysical Data Center, accessed 17 Nov 2015, doi:https://doi.org/10.7289/V5J1012Q.

Oleson, K., and Coauthors, 2010: Technical description of version 4.0 of the Community Land Model (CLM). National Center for Atmospheric Research Tech. Note NCAR/TN-478+STR, 257 pp., doi:https://doi.org/10.5065/D6FB50WZ.

Palmer, P. L., 1988: The SCS snow survey water supply forecasting program: Current operations and future directions. *Proc. 56th Annual Meeting, Western Snow Conference*, Kalispell, MT, Western Snow Conference, 43–51. [Available online at http://westernsnowconference.org/sites/westernsnowconference.org/PDFs/1988Palmer.pdf.]

Pandey, G. R., D. R. Cayan, and K. P. Georgakakos, 1999: Precipitation structure in the Sierra Nevada of California during winter. *J. Geophys. Res.*, 104, 12 019–12 030, doi:https://doi.org/10.1029/1999JD900103.

Park, S., and C. S. Bretherton, 2009: The University of Washington shallow convection and moist turbulence schemes and their impact on climate simulations with the Community Atmosphere Model. *J. Climate*, 22, 3449–3469, doi:https://doi.org/10.1175/2008JCLI2557.1.

Park, S., C. S. Bretherton, and P. J. Rasch, 2014: Integrating cloud processes in the Community Atmosphere Model, version 5. *J. Climate*, 27, 6821–6856, doi:https://doi.org/10.1175/JCLI-D-14-00087.1.

Pierce, D. W., and D. R. Cayan, 2013: The uneven response of different snow measures to human-induced climate warming. *J. Climate*, 26, 4148–4167, doi:https://doi.org/10.1175/JCLI-D-12-00534.1.

Ralph, F. M., P. J. Neiman, and G. A. Wick, 2004: Satellite and CALJET aircraft observations of atmospheric rivers over the eastern North Pacific Ocean during the winter of 1997/98. *Mon. Wea. Rev.*, 132, 1721–1745, doi:https://doi.org/10.1175/1520-0493(2004)132<1721:SACAOO>2.0.CO;2.

Rupp, D. E., P. W. Mote, N. L. Bindoff, P. A. Stott, and D. A. Robinson, 2013: Detection and attribution of observed changes in Northern Hemisphere spring snow cover. *J. Climate*, 26, 6904–6914, doi:https://doi.org/10.1175/JCLI-D-12-00563.1.

Saha, S., and Coauthors, 2014: The NCEP Climate Forecast System version 2. *J. Climate*, 27, 2185–2208, doi:https://doi.org/10.1175/JCLI-D-12-00823.1.

Salzmann, N., and L. O. Mearns, 2012: Assessing the performance of multiple regional climate model simulations for seasonal mountain snow in the upper

Colorado River basin. *J. Hydrometeor.*, 13, 539–556, doi:https://doi.org/10.1175/2011JHM1371.1.

Seaber, P. R., F. P. Kapinos, and G. L. Knapp, 1987: Hydrologic unit maps. U.S. Geological Survey Water-Supply Paper 2294, 63 pp. [Available online at http://pubs.usgs.gov/wsp/wsp2294/pdf/wsp_2294.pdf.]

Serreze, M. C., M. P. Clark, R. L. Armstrong, D. A. McGinnis, and R. S. Pulwarty, 1999: Characteristics of the western United States snowpack from snowpack telemetry (SNOTEL) data. *Water Resour. Res.*, 35, 2145–2160, doi:https://doi.org/10.1029/1999WR900090.

Stewart, W. C., 1996: Economic assessment of the ecosystem. In Sierra Nevada Ecosystem Project: Final report to Congress—Status of the Sierra Nevada, Vol. III: Assessments, commissioned reports, and background information. University of California, Davis, Centers for Water and Wildland Resources Wildland Resources Center Rep. 38 (section 23), 91 pp. [Available online at http://pubs.usgs.gov/dds/dds-43/VOL_III/VIII_C23.PDF.]

Tanaka, S. K., and Coauthors, 2006: Climate warming and water management adaptation for California. *Climatic Change*, 76, 361–387, doi:https://doi.org/10.1007/s10584-006-9079-5.

Taylor, M. A., and A. Fournier, 2010: A compatible and conservative spectral element method on unstructured grids. *J. Comput. Phys.*, 229, 5879–5895, doi:https://doi.org/10.1016/j.jcp.2010.04.008.

Taylor, M. A., J. Tribbia, and M. Iskandarani, 1997: The spectral element method for the shallow water equations on the sphere. *J. Comput. Phys.*, 130, 92–108, doi:https://doi.org/10.1006/jcph.1996.5554.

Thornton, P., M. Thornton, B. Mayer, N. Wilhelmi, Y. Wei, R. Devarakonda, and R. Cook, 2014: Daymet: Daily Surface Weather Data on a 1-km Grid for North America, version 2. Oak Ridge National Laboratory Distributed Active Archive Center. Subset used: 1980–2005, accessed 1 November 2014, doi:https://doi.org/10.3334/ORNLDAAC/1219.

Ullrich, P. A., 2014: SQuadGen: Spherical quadrilateral grid generator. University of California, Davis, Climate and Global Change Group software. [Available online at http://climate.ucdavis.edu/squadgen.php.]

Ullrich, P. A., and M. A. Taylor, 2015: Arbitrary-order conservative and consistent remapping and a theory of linear maps: Part I. *Mon. Wea. Rev.*, 143, 2419–2440, doi:https://doi.org/10.1175/MWR-D-14-00343.1.

Varhola, A., N. C. Coops, M. Weiler, and R. D. Moore, 2010: Forest canopy effects on snow accumulation and ablation: An integrative review of empirical results. *J. Hydrol.*, 392, 219–233, doi:https://doi.org/10.1016/j.jhydrol.2010.08.009.

Wallace, J. M., and D. S. Gutzler, 1981: Teleconnections in the geopotential height field during the Northern Hemisphere winter. *Mon. Wea. Rev.*, 109,

784–812, doi:https://doi.org/10.1175/1520-0493(1981)109<0784:TITGHF>2.0.CO;2.

Wang, S.-Y., L. Hipps, R. R. Gillies, and J.-H. Yoon, 2014: Probable causes of the abnormal ridge accompanying the 2013–2014 California drought: ENSO precursor and anthropogenic warming footprint. *Geophys. Res. Lett.*, 41, 3220–3226, doi:https://doi.org/10.1002/2014GL059748.

Wehner, M. F., and Coauthors, 2014: The effect of horizontal resolution on simulation quality in the Community Atmospheric Model, CAM5.1. *J. Adv. Model. Earth Syst.*, 6, 980–997, doi:https://doi.org/10.1002/2013MS000276.

Wise, E. K., 2012: Hydroclimatology of the US Intermountain West. *Prog. Phys. Geogr.*, 36, 458–479, doi:https://doi.org/10.1177/0309133312446538.

Xia, Y., and Coauthors, 2012a: Continental-scale water and energy flux analysis and validation for North American Land Data Assimilation System project phase 2 (NLDAS-2): 1. Intercomparison and application of model products. *J. Geophys. Res.*, 117, D03109, doi:https://doi.org/10.1029/2011JD016048.

Xia, Y., and Coauthors, 2012b: Continental-scale water and energy flux analysis and validation for North American Land Data Assimilation System project phase 2 (NLDAS-2): 2. Validation of model-simulated streamflow. *J. Geophys. Res.*, 117, D03110, doi:https://doi.org/10.1029/2011JD016051.

Yang, Z.-L., X. Cai, G. Zhang, A. A. Tavakoly, Q. Jin, L. H. Meyer, and X. Guan, 2011: The Community Noah Land Surface Model with Multi-Parameterization Options (Noah-MP): Technical description. The University of Texas at Austin Dept. of Geological Sciences Center for Integrated Earth System Science Tech. Rep., 72 pp. [Available online at http://www.jsg.utexas.edu/noah-mp/files/Noah-MP_Technote_v0.2.pdf.]

Yen, Y.-C., 1965: Heat transfer characteristics of naturally compacted snow. Cold Regions Research and Engineering Laboratory Research Rep. 166, 14 pp. [Available online at http://acwc.sdp.sirsi.net/client/search/asset/1013065.]

Yongjiu, D., and Z. Qingcun, 1997: A land surface model (IAP94) for climate studies part I: Formulation and validation in off-line experiments. *Adv. Atmos. Sci.*, 14, 433–460, doi:https://doi.org/10.1007/s00376-997-0063-4.

Zarzycki, C. M., and C. Jablonowski, 2014: A multidecadal simulation of Atlantic tropical cyclones using a variable-resolution global atmospheric general circulation model. *J. Adv. Model. Earth Syst.*, 6, 805–828, doi:https://doi.org/10.1002/2014MS000352.

Zarzycki, C. M., C. Jablonowski, and M. A. Taylor, 2014a: Using variable resolution meshes to model tropical cyclones in the Community Atmosphere Model. *Mon. Wea. Rev.*, 142, 1221–1239, doi:https://doi.org/10.1175/MWR-D-13-00179.1.

Zarzycki, C. M., M. N. Levy, C. Jablonowski, J. R. Overfelt, M. A. Taylor, and P. A. Ullrich, 2014b: Aquaplanet experiments using CAM's variable-resolution dynamical core. *J. Climate*, 27, 5481–5503, doi:https://doi.org/10.1175/JCLI-D-14-00004.1.

Zarzycki, C. M., C. Jablonowski, D. R. Thatcher, and M. A. Taylor, 2015: Effects of localized grid refinement on the general circulation and climatology in the Community Atmosphere Model. *J. Climate*, 28, 2777–2803, doi:https://doi.org/10.1175/JCLI-D-14-00599.1.